

Quarterly Technical Report

Solid State Research

2003:2

Lincoln Laboratory
MASSACHUSETTS INSTITUTE OF TECHNOLOGY
LEXINGTON, MASSACHUSETTS



Prepared for the Department of the Air Force under Contract F19628-00-C-0002.

Approved for public release; distribution is unlimited.

20031105 002


This report is based on studies performed at Lincoln Laboratory, a center for research operated by Massachusetts Institute of Technology. The work was sponsored by the Department of the Air Force under Contract F19628-00-C-0002.

This report may be reproduced to satisfy needs of U.S. Government agencies.

The ESC Public Affairs Office has reviewed this report, and it is releasable to the National Technical Information Service, where it will be available to the general public, including foreign nationals.

This technical report has been reviewed and is approved for publication.

FOR THE COMMANDER


Gary Tutungian
Administrative Contracting Officer
Plans and Programs Directorate
Contracted Support Management

Non-Lincoln Recipients

PLEASE DO NOT RETURN

Permission is given to destroy this document
when it is no longer needed.

Massachusetts Institute of Technology
Lincoln Laboratory

Solid State Research

Quarterly Technical Report
2003:2

1 February — 30 April 2003

Issued 17 October 2003

Approved for public release; distribution is unlimited.

TABLE OF CONTENTS

Abstract	iii
List of Illustrations	vii
List of Tables	xiii
Introduction	xv
Reports on Solid State Research	xvii
Organization	xxv
 1. QUANTUM ELECTRONICS	
1.1 Development of a UV LED-Based Biosensor	1
 2. ELECTRO-OPTICAL MATERIALS AND DEVICES	
2.1 Wafer Fusion of GaSb to GaAs	9
 3. SUBMICROMETER TECHNOLOGY	
3.1 Fabrication of DAST Electro-optic Waveguides Using Graphoepitaxial Crystal Growth	15
3.2 Angle-Resolved Scattering Measurement System for 157-nm Optics	19
 4. BIOSENSOR AND MOLECULAR TECHNOLOGIES	
4.1 Biosilicon Integration	27
 5. ADVANCED IMAGING TECHNOLOGY	
5.1 CMOS Timing Chip for Three-Dimensional Imaging with Geiger-Mode Avalanche Photodiodes	37

6. ANALOG DEVICE TECHNOLOGY

- 6.1 Quantum Flux Parametron as a Readout Element for a Persistent-Current Qubit 43

7. ADVANCED SILICON TECHNOLOGY

- 7.1 New SPICE Model Utilizing the Body-Source Built-In Potential Lowering of SOI MOSFETs 51

LIST OF ILLUSTRATIONS

Figure No.		Page
1-1	Schematic of generic biological agent detection system. The trigger must continuously operate and activate the sample collector whenever a threatening aerosol is present. The collector concentrates the aerosol particles, typically into a liquid, for presentation to the identifier. In the event of a positive identification a further confirmation identification procedure is performed.	1
1-2	Illustration showing better protection by a large array of inexpensive detectors than by a single very high performance, expensive detector. For a point detector to sense a biological agent cloud, that cloud must pass over the detector; assuming some minimum level of detector performance a large array of detectors is more likely to be exposed to, and hence detect, a biological agent cloud than is a single detector.	2
1-3	Minimum detectable concentration as a function of average optical power for bioparticle cross sections at fluorescence excitation wavelengths of 290, 340, and 400 nm. See Equation (1.4) and Table 1-1.	4
1-4	Schematic for UV light-emitting diode based biological agent sensor trigger.	5
1-5	(a) Photograph of experimental apparatus for measuring biological particle signals utilizing a laser diode light source, and (b) oscilloscope traces of elastic scattering and fluorescence signals from single <i>Bacillus globigii</i> spores.	6
2-1	Scanning electron micrograph (SEM) of cleaved cross section of GaSb and GaAs wafers fused without pressure at 576 °C for 140 h at (a) low magnification and (b) high magnification.	10
2-2	SEMs of cleaved cross section of lattice-matched GaSb/GaInAsSb/InAsSb/GaSb heterostructure fused to GaAs at 400 °C for 53 h with pressure: (a) full image of GaSb/GaInAsSb/InAsSb heterostructure, GaSb substrate, and GaAs wafer; and (b) enlarged view of fused interface.	11
2-3	X-ray diffraction of GaSb/GaInAsSb/GaSb heterostructure fused (a) to a smooth GaAs wafer with pressure and (b) to a grooved GaAs wafer without pressure.	12

LIST OF ILLUSTRATIONS (Continued)

Figure No.		Page
2-4	300-K photoluminescence of GaSb/GaInAsSb/GaSb heterostructures fused to GaAs with and without pressure.	12
3-1	Weight of molten DAST in flowing dry nitrogen as a function of time for several temperatures. It is assumed that the weight loss is directly related to decomposition.	15
3-2	DAST melted and solidified on SiO ₂ . (a) Schematic diagram showing the cross section of a substrate with the grating on the left and the unpatterned surface on the right. (b) Optical micrograph of DAST using polarized light as indicated. (c) Optical micrograph of the same region shown in (b) but with the illuminating polarization changed. Note the random orientation of the crystallites on the unpatterned surface and the consistent orientation in the grating region.	16
3-3	Distribution of c-axis of crystallites as a function of angle from the substrate normal. Half of the DAST crystalline volume has its c-axis less than 4.5° from substrate normal and 90% is within 9°. The inset shows a schematic diagram of crystallites with their c-axis a few degrees from the substrate normal.	17
3-4	(a) Optical micrograph of DAST waveguide 4 μm deep and 15 μm wide, which was seeded from crystals on either side. The crossed gratings were over-coated with 100 nm of Cr before DAST deposition and used to electrically contact the crystal. (b) Schematic cross section of substrate shown in (a). The lower Si substrate is used to give a well-defined cleaving plane normal to the waveguides.	18
3-5	Schematic drawing of 157-nm angle-resolved scattering measurement system. A 2× magnification system is used to image a coherently illuminated pinhole. Two separate detectors are employed for small- and large-angle scattering measurements. The entire beam path is purged with nitrogen.	20

LIST OF ILLUSTRATIONS (Continued)

Figure No.		Page
3-6	Simulated aerial image for three different radii of the entrance window using a 100- μm pinhole in the object plane. A semi-analytic scalar field propagation model was used to predict the aerial image. The scalar field at a given reference plane is first discretized. The resulting field at a new position along the optic axis is a linear superposition of the field generated for each discretized region, each of which can be written in terms of Lommel functions [16]. Also shown is the contribution from secondary reflections within the lens. This fraction is modeled by including a second lens at the pupil plane with a focal length of 60.8 mm (the combination of two lenses of 654 and 67 mm) and transmission factor of 0.047^2 to account for Fresnel losses. The inset graph shows the predicted signal intensity at 0.5° from the optical axis as the entrance window radius is varied from the optimal value of 1.25 mm, where the aperture radius is equal to the radius of the primary lobe.	21
3-7	Comparison of predicted and measured background signal for the 2 \times imaging system using a 100- μm pinhole in the object plane. The predicted curve is calculated by convolving the aerial image that is formed when the entrance window is 2 mm larger than the radius of the first lobe and the detector has a 2-mm-diam circular aperture.	22
3-8	Atomic force microscopy profile of a 12.5- μm period grating etched in CaF_2 . Significant redeposition of material occurred along the sidewalls during the etching of the grating. These features repeat at one-half the grating period. The amplitude of the grating, Δ_1 , is one half of the 6.25-nm etched depth. The amplitude of the steps of redeposited material, Δ_2 , is one half of the 10-nm step height.	23
3-9	Contour plot of the diffracted field from the grating shown in Figure 3-8, encompassing the first-order lobes. The numbers in the plot represent the log of the intensity in relative units. The x - and y -axes specify the displacement of the photomultiplier sensor from the center of the imaged beam.	23

LIST OF ILLUSTRATIONS (Continued)

Figure No.		Page
3-10	Measured intensity of a single line scan that transverses the diffracted orders formed by the grating. The scan was extended to encompass the second-order lobes. Also shown are the expected locations of each peak and the expected intensity of the first lobe. For a perfect grating, this intensity level is approximately equal to the square of the product of the wave number times the amplitude of the grating. The measured intensity is lower by a factor of 5, presumably because of the loss of energy into the second order.	24
4-1	Bilayer lipid membrane (BLM) structure and support.	27
4-2	Micromachined silicon nitride apertures: (a) diagram of back side of chip, (b) scanning electron micrograph (SEM) of front side of chip showing aperture, and (c) SEM of back side of chip showing closeup of aperture.	28
4-3	Conceptual schematics of (a) membrane maker and (b) BLM formation procedure.	29
4-4	Test jig for conducting membrane capacitance measurements.	30
4-5	Membrane formation as observed in optical microscope. Phospholipid is phosphatidyl ethanolamine (10 mg/mL) in chloroform; aqueous solution is 0.1M NaCl at room temperature.	30
4-6	Examples of measured capacitance of membranes: (a) Triangular voltage input signal and square current output signal across membrane. Input is applied and output measured with a Keithley 6430 source meter. (b) Measured current and capacitance across membrane ($I = C dV/dt$) formed in 140- μm -diam aperture. Lipid is $\sim 3\text{-}\mu\text{L}$ phosphatidyl ethanolamine (5 mg/mL) in <i>n</i> -decane. Aqueous solution is 0.1M KCl at 30°C. Back-side fluid pressure is varied with a threaded syringe. The application of positive pressure increases membrane thickness and decreases capacitance; suction decreases membrane thickness by pulling excess lipid away from the aperture and increases capacitance. (c) Measured current and capacitance across membrane formed in 80- μm -diam aperture. Lipid is $\sim 3\text{-}\mu\text{L}$ phosphatidyl ethanolamine (10 mg/mL) in <i>n</i> -decane. Aqueous solution is 0.1M KCl at 30°C.	31

LIST OF ILLUSTRATIONS (Continued)

Figure No.		Page
4-7	Structure of vesicle (liposome).	33
4-8	(a) Micromachined structure and (b) liposome formation and ion-channel-current measurement.	34
4-9	Phase contrast micrographs of vesicles generated from rehydrated dried lipid films: (a) Lipid is phosphatidyl ethanolamine at 10 mg/mL in chloroform, 0.5 μ L deposited on Pt electrode, rehydrated in distilled water with 2 V_{dc} across 2-mm gap. Image is taken at the corner of Pt electrode. (b) Silicon nitride aperture seen from above through upper ITO electrode. (c)–(e) Lipid is DOPG-Na at 10 mg/mL, 0.5 μ L deposited on ITO lower electrode, rehydrated in distilled water. Shown are (c) vesicle before attachment to aperture, 7 V_{dc} across 3-mm gap, (d) vesicle attached to aperture, 5 V_{dc} across 3-mm gap, and (e) large unattached vesicle, 5 V_{dc} across 3-mm gap.	35
5-1	Logic diagram of pixel circuit of ladar focal plane.	38
5-2	D flip-flop circuit that forms the building block of the pixel counter.	39
5-3	Logic diagram of ring oscillator that produces the master clock and the 90°-delayed clock.	39
5-4	Photograph of 32 \times 32 CMOS timing chip.	41
5-5	Photograph of single pixel of the CMOS timing chip.	41
5-6	Grey-scale image showing the state of the vernier timing bits in response to electronic triggering of the timing chip using the DISARM signal.	42
6-1	(a) Schematic of quantum flux parametron (QFP) comparator. The comparator includes the QFP arms, QFP spine and offset current, QFP exciter line, and QFP readout superconducting quantum interference device (SQUID). The comparator is used to read out the state of a persistent current qubit. The qubit is biased, and it induces a current into the spine, which is subsequently discriminated by the QFP. (b) Grey zone for a QFP comparator. The ideal grey zone is a step function. The presence of noise results in a distribution of spine currents, which leads to a grey zone when the comparator output is averaged over many trials. The slope of the grey zone at the 50% point, i_{s0} , is a figure of merit for the comparator.	44

LIST OF ILLUSTRATIONS (Continued)

Figure No.		Page
6-2	Grey zone slope as a function of temperature (right axis). The inset is a grey zone at temperature $T = 2$ K. The slope is the plotted $T = 2$ K point. The corresponding sensitivity is plotted as a function of temperature (left axis). The slope and sensitivity saturate at around 1 K, likely indicating that the on-chip resistor is heating the sample locally.	47
6-3	(a) Readout of QFP comparator as a function of the qubit bias current (~ 1 -h duration). The data as measured (red trace) exhibits a $1/f$ type noise spectrum. A lock-in type technique is used to remove this low-frequency fluctuation (blue trace). Traces are offset for clarity in presentation. The general increase in probability of logic 1 is due to the mutual coupling of the qubit bias current to the spine. (b) Power spectrum for the uncompensated data in (a) with the mutual coupling contribution removed. The data exhibit a $1/f$ type noise with a corner frequency of 200 mHz, corresponding to a characteristic time of 5 s.	48
7-1	ΔV_{bi} vs V_{GS} . ΔV_{bi} is caused by vertical coupling from front gate to back gate. It can be experimentally determined using body-contacted devices. $L_G = 0.5 \mu\text{m}$, $T_{Si} = 40 \text{ nm}$, $N_{ch} = 6 \times 10^{17} \text{ cm}^{-3}$, $T_{BOX} = 200 \text{ nm}$.	52
7-2	ΔV_{bi} vs channel implant. ΔV_{bi} depends linearly on channel doping with a slope proportional to T_{Si}^2 . It is an index of the degree of full depletion. $L_G = 1 \mu\text{m}$, $T_{BOX} = 85 \text{ nm}$, $V_{GS} = 0.1 \text{ V}$, $V_{bGS} = 0 \text{ V}$.	53
7-3	(a) V_T and ΔV_{bi} vs L_G . Drain field penetration causes roll-off and raises ΔV_{bi} for the short-channel device. (b) ΔV_{bi} vs V_{bGS} . Back-gate effect on ΔV_{bi} (the slope in this figure) for the short-channel device is also reduced because of the charge sharing. C_{BOX} is the buried oxide capacitance, and C_{Si} is the capacitance of the depleted SOI silicon film. $V_{GS} = 0.4 \text{ V}$, $T_{Si} = 40 \text{ nm}$, $N_{ch} = 6 \times 10^{17} \text{ cm}^{-3}$, $T_{BOX} = 200 \text{ nm}$.	54
7-4	I_{BS} vs V_{BS} . ΔV_{bi} determines the diode current-voltage and therefore the body potential of silicon-on-insulator (SOI) devices. It is the link between partially depleted (PD) and fully depleted models.	55
7-5	Measured (points) and simulated (lines) current-voltage curves for two transistors from Lincoln Laboratory's fully depleted SOI CMOS process.	56

LIST OF TABLES

Table No.		Page
1-1	Description of Variables Used in Equation (1.4) and the Values Assumed for These Variables in Figure 1-3	4
4-1	Parameters for Optimal Membrane Formation Time and Stability	32

INTRODUCTION

1. QUANTUM ELECTRONICS

A test bed using UV light-emitting diodes for detecting biological agent aerosols has been designed. An experimental apparatus was used to measure the elastic scattering and fluorescence signals from single bacterial spores illuminated by low-power 408-nm laser diode radiation.

2. ELECTRO-OPTICAL MATERIALS AND DEVICES

GaSb/GaInAsSb/GaSb epilayers have been transferred to GaAs wafers by atomic wafer fusion without mechanical pressure at temperatures as low as 350°C, followed by GaSb substrate removal. The fusion without pressure results in significantly improved structural and optical properties.

3. SUBMICROMETER TECHNOLOGY

Lithographically defined microstructures have been used to control the growth of the organic crystalline electro-optic material DAST on silicon substrates. Mach Zehnder interferometer modulators have been built utilizing this technique, and measurements indicate that the electro-active coefficient of DAST is an order of magnitude greater than that of LiNbO₃.

An angle-resolved scattering detection system has been designed and implemented for use at 157-nm wavelength. In this test bed, scattered rays can be collected to 4° from the directional ray of the specularly transmitted beam, corresponding to spatial wavelengths of surface roughness <2 μm, over a dynamic range of 7 orders of magnitude; angular sensitivity can be extended to 0.5°, but with a dynamic range of 5 orders of magnitude.

4. BIOSENSOR AND MOLECULAR TECHNOLOGIES

Two methods have been developed for forming bilayer lipid membranes—the lipid droplet and the vesicle formation approaches. Demonstrations of both methods have been conducted, and for the lipid droplet approach, optimal parameters to minimize membrane formation time have been determined.

5. ADVANCED IMAGING TECHNOLOGY

An all-digital timing chip for ladar focal planes using Geiger-mode avalanche photodiodes has been demonstrated. The chip is scalable to larger formats, operates at high frame rates, and supports photon flight time measurements with 0.5-ns resolution.

6. ANALOG DEVICE TECHNOLOGY

The quantum flux parametron (QFP) comparator is a promising readout element for a persistent-current qubit. The QFP grey zone width decreases as the temperature is decreased; a width of 300 nA is achieved reproducibly at temperatures of 300 mK.

7. ADVANCED SILICON TECHNOLOGY

A new SPICE model for silicon-on-insulator transistors has been developed and released to industry. The model utilizes the built-in potential in a new way to accurately describe both fully and partially depleted devices.

REPORTS ON SOLID STATE RESEARCH

1 FEBRUARY THROUGH 30 APRIL 2003

PUBLICATIONS

- | | | |
|---|---|--|
| Wavelength Beam Combining of
Ytterbium Fiber Lasers | S. J. Augst
A. K. Goyal
R. L. Aggarwal
T. Y. Fan
A. Sanchez | <i>Opt. Lett.</i> 28 , 331 (2003) |
| Exceptionally High Voltage
Schottky Diamond Diodes and
Low Boron Doping | J. E. Butler*
M. W. Geis
K. E. Krohn
J. M. Lawless
S. J. Deneault
T. M. Lyszcza
D. Flechtner*
R. Wright* | <i>Semicond. Sci. Technol.</i>
18 , S67 (2003) |
| Effects of CMOS Process Fill
Patterns on Spiral Inductors | C. L. Chen | <i>Microw. Opt. Technol. Lett.</i>
36 , 462 (2003) |
| AlGaAs-InGaAs Slab-Coupled
Optical Waveguide Lasers | J. P. Donnelly
R. K. Huang
J. N. Walpole
L. J. Missaggia
C. T. Harris
J. J. Plant
R. J. Bailey
D. E. Mull
W. D. Goodhue
G. W. Turner | <i>IEEE J. Quantum Electron.</i>
39 , 289 (2003) |
| Large-Area Patterning of ~50 nm
Structures on Flexible Substrates
Using Near-Field 193 nm Radiation | R. R. Kunz
M. Rothschild
M. S. Yeung* | <i>J. Vac. Sci. Technol. B</i> 21 , 78
(2003) |

*Author not at Lincoln Laboratory.

Current Mapping of GaN Films
by Conductive Atomic Force
Microscopy

A. A. Pomarico*
D. Huang*
J. Dickinson*
A. A. Baski*
R. Cingolani*
H. Morkoç*
R. Molnar

Appl. Phys. Lett. **82**, 1890
(2003)

High-Speed Electronically
Shuttered Solid-State Imager
Technology

R. K. Reich
D. D. Rathman
D. M. O'Mara
D. J. Young
A. H. Loomis
E. J. Kohler
R. M. Osgood
R. A. Murphy
M. K. Rose
R. Berger
S. A. Watson

Rev. Sci. Instrum. **74**, 2027
(2003)

PRESENTATIONS[†]

Intermodulation Distortion and
Third Harmonic Generation in
YBCO Films of Varying Oxygen
Content

D. Oates
S. H. Park
M. A. Hein*
P. J. Hurst*
R. G. Humphreys*

Office of Naval Research
Annual Review,
Melbourne, Florida,
2-5 February 2003

Widely Tunable, Aluminum-Free,
GaSb-Based, Mid-Infrared
Semiconductor Lasers

A. K. Goyal
G. W. Turner
A. Sanchez
M. J. Manfra
P. J. Foti
P. O'Brien

OSA Topical Meeting on
Advanced Solid State
Photonics,
San Antonio, Texas,
2-5 February 2003

*Author not at Lincoln Laboratory.

[†] Titles of presentations are listed for information only. No copies are available for distribution.

Miniature, High-Power 355-nm Laser System	J. J. Zayhowski A. L. Wilson	OSA Topical Meeting on Advanced Solid State Photonics, San Antonio, Texas, 2-5 February 2003
Aerosol Triggers	J. Hybl	Technical Seminar, University of Colorado, Boulder, Colorado, 11 February 2003
Biological Agent Detection	T. H. Jeys M. Hollis	Optical Sensing for Homeland Security Forum, Washington, D.C., 19-20 February 2003
Angle Resolved Scattering Measurements of Polished CaF_2 Surfaces and Optical Coatings at 157 nm	T. Bloomstein D. Hardy M. Rothschild	SPIE Microlithography, Santa Clara, California, 23-28 February 2003
Contamination Rates of Optical Surfaces at 157 nm: Impurities Outgassed from Construction Materials and from Photoresists	T. M. Bloomstein J. H. C. Sedlacek S. T. Palmacci D. E. Hardy V. Liberman M. Rothschild	SPIE Microlithography, Santa Clara, California, 23-28 February 2003
Quantum Efficiency of PAG Decomposition in Different Polymer Matrices at Advanced Lithographic Wavelengths	T. H. Fedynyshyn R. F. Sinta W. A. Mowers A. Cabral	SPIE Microlithography, Santa Clara, California, 23-28 February 2003
Limits of Strong Phase Shift Patterning for Device Research	M. Fritze R. Mallen D. Yost B. Wheeler	SPIE Microlithography, Santa Clara, California, 23-28 February 2003

193 nm Lithography: Fundamentals and Issues	R. R. Kunz	SPIE Microlithography, Santa Clara, California, 23-28 February 2003
Monolithic Detector Array Comprising >1000 Aerial Image Sensing Elements	R. R. Kunz D. D. Rathman S. J. Spector M. Yeung*	SPIE Microlithography, Santa Clara, California, 23-28 February 2003
Accelerated Damage to Blank and AR-Coated CaF ₂ Surfaces under 157-nm Laser Irradiation	V. Liberman M. Rothschild N. Efremow S. T. Palmacci J. H. C. Sedlacek A. Grenville*	SPIE Microlithography, Santa Clara, California, 23-28 February 2003
Ambient Effects on the Laser Durability of 157-nm Optical Coatings	V. Liberman M. Rothschild N. Efremow S. Palmacci J. Sedlacek A. Grenville*	SPIE Microlithography, Santa Clara, California, 23-28 February 2003
Immersion Liquids for Lithography in the Deep Ultraviolet	M. Switkes R. R. Kunz M. Rothschild R. F. Sinta P. M. Gallagher- Wetmore* V. J. Krukonis*	SPIE Microlithography, Santa Clara, California, 23-28 February 2003
Preliminary Microfluidic Simulation for Immersion Lithography	A. Wei* G. Nellis* A. Abdo* R. Engelstad* C.-F. Chen M. Rothschild M. Switkes	SPIE Microlithography, Santa Clara, California, 23-28 February 2003

*Author not at Lincoln Laboratory.

Simulation Study of Process
Latitude for Liquid Immersion
Lithography

S.-Y. Yeon*
D. C. Cole*
M. Yeung*
E. Barouch*
M. Rothschild
M. Switkes

SPIE Microlithography,
Santa Clara, California,
23-28 February 2003

A Scalable CMOS Readout Circuit
Architecture for Photon-Counting
Applications Using Geiger-Mode
Avalanche Photodiodes

A. Stern
B. F. Aull
B. B. Kosicki
R. R. Reich

Meeting of the Military
Sensing Symposia Specialty
Group on Passive Sensors,
Tucson, Arizona,
24-28 February 2003

Dense-Only Phase Shift Template
Lithography

M. Fritze
B. Tyrrell

SPIE Advanced
Microelectronic
Manufacturing,
Santa Clara, California,
27-28 February 2003

Optical Sampling for Analog-to-
Digital Conversion

J. C. Twichell

Lincoln Laboratory
Technical Seminar Series,
University of California,
San Diego, California,
28 February 2003

Wavelength and Coherently
Combined Fiber Laser Arrays

T. Y. Fan

Optics and Quantum
Electronics Seminar,
Massachusetts Institute
of Technology,
Cambridge, Massachusetts,
12 March 2003

Optical Sampling for High-Speed,
High-Resolution Analog-to-Digital
Converters

P. W. Juodawlkis
J. J. Hargreaves
R. D. Younger
R. C. Williamson
J. C. Twichell

Technical Seminar,
Georgia Institute
of Technology,
Atlanta, Georgia,
20 March 2003

*Author not at Lincoln Laboratory.

Microscale Electric Induction
Machines for Power Applications

C. Livermore*
S. Umans*
J. Lang*
T. M. Lyszczarz
A. R. Forte

Electrostatics Conference,
Heriot-Watt University,
Edinburgh, Scotland,
23-27 March 2003

Magnetic Relaxation and
Anisotropy Effects on High-
Frequency Permeability

G. F. Dionne

IEEE International Magnetics
Conference,
Boston, Massachusetts,
30 March–3 April 2003

Photonic Components for RF
Filtering and Wide-Band Antenna
Nulling

M. W. Geis
S. Spector
R. Williamson
T. M. Lyszczarz
S. Johnson
M. Povinelli*

28th Annual GOMACTech
Conference,
Tampa, Florida,
31 March–3 April 2003

Laser-Based RF Precision
Oscillators

J. J. Hargreaves
S. J. Augst
D. L. Spears
J. C. Twichell
C. Freed
T. Y. Fan

28th Annual GOMACTech
Conference,
Tampa, Florida,
31 March–3 April 2003

Optical Sampling for Analog-to-
Digital Conversion

P. W. Juodawlkis
J. J. Hargreaves
R. D. Younger
R. C. Williamson
G. Betts

28th Annual GOMACTech
Conference,
Tampa, Florida,
31 March–3 April 2003

*Author not at Lincoln Laboratory.

Technologies, Circuits, and
Applications That Enable and
Demonstrate Efficient, Mixed-
Signal Microsystems

C. L. Keast
C-L. Chen
M. Gouker
L. Johnson
J. Sage
D. Santiago
M. Seaver
C. Howard
P. Monticciolo
W. Song
M. Vai

28th Annual GOMACTech
Conference,
Tampa, Florida,
31 March–3 April 2003

High- T_c Microwave Materials and
Applications

D. E. Oates

Invited Seminar, Naval
Surface Warfare Center,
Bethesda, Maryland,
8 April 2003

Fabrication, Integration and Design
of Superconducting Quantum
Computing Devices

K. Berggren
P. Cho
J. Sage
W. Oliver

Seminar, Physics Department,
Rice University,
Houston, Texas,
21 April 2003

Development of a UV LED Based
Biosensor

T. H. Jeys
L. Desmarais
E. J. Lynch
J. R. Ochoa

AeroSense—Technologies and
Systems for Defense and
Security,
Orlando, Florida,
21-25 April 2003

Fabrication of Three-Dimensional
Integrated Circuits by Layer
Transfer of Fully Depleted SOI
Circuits

J. A. Burns
C. L. Keast
P. W. Wyatt
D. R. Yost
K. Warner

Materials Research Society
Spring Meeting,
San Francisco, California,
21-25 April 2003

Recombination Parameters in
InGaAsSb Epitaxial Layers for
Thermophotovoltaic Applications

C. A. Wang
R. J. Kumar*
R. J. Gutmann*
J. M. Borrego*
P. S. Dutta*
R. U. Martinelli*
G. Nichols*

Materials Research Society
Spring Meeting,
San Francisco, California,
21-25 April 2003

Wafer Fusion of GaSb and GaAs

C. A. Wang
Z. L. Liao
D. A. Shiau
P. M. Nitishin

Materials Research Society
Spring Meeting,
San Francisco, California,
21-25 April 2003

Effect of Growth Interruption on the
Properties of GaInAsSb/AlGaAsSb
Heterostructures and the
Performance of Thermophoto-
voltaic Devices

C. A. Wang
D. A. Shiau
M. K. Connors
L. R. Danielson*
G. Nichols*
D. Donetsky*
S. Anikeev*
G. Belenky*

Materials Research Society
Spring Meeting,
San Francisco, California,
21-25 April 2003

Fabrication and Characterization of
Wafer-Bonded GaInAsSb Epitaxy
for Monolithically Interconnected
Thermophotovoltaic Devices

C. A. Wang
D. A. Shiau
P. W. O'Brien
P. G. Murphy
R. K. Huang

Materials Research Society
Spring Meeting,
San Francisco, California,
21-25 April 2003

Microscale Electric Induction
Machines for Power Applications

C. Livermore*
S. D. Umans*
J. Lang*
A. R. Forte
T. M. Lyszczarz

Annual Symposium of
Collaborative Technology
Alliances,
Adelphi, Maryland,
28 April–1 May 2003

Fabrication, Integration and Design
of Superconducting Quantum
Computing Devices

K. Berggren
P. Cho
J. Sage
W. Oliver

Seminar, MIT Department
of Electrical Engineering
and Computer Science,
Cambridge, Massachusetts,
29 April 2003

*Author not at Lincoln Laboratory.

ORGANIZATION

SOLID STATE DIVISION

D. C. Shaver, Head
R. W. Ralston, Associate Head
N. L. DeMeo, Jr., Assistant
Z. J. Lemnios, Senior Staff
K. J. Challberg, Administrative Staff
J. D. Pendergast, Administrative Staff
L. K. Soule-Hinds, Administrative Staff

SUBMICROMETER TECHNOLOGY

M. Rothschild, Leader
T. M. Lyszczarz, Assistant Leader
T. H. Fedynyshyn, Senior Staff
R. R. Kunz, Senior Staff

Astolfi, D. K.
Bloomstein, T. M.
Cann, S. G.
Creel, C. R.
DiNatale, W. F.
Efremow, N. N., Jr.
Geis, M. W.
Goodman, R. B.
Krohn, K. E.
Leibowitz, F. L.

Lennon, D. M.
Liberman, V.
Palmacci, S. T.
Pottebaum, I. S.
Sedlacek, J. H. C.
Spector, S. J.
Stallman, J. B.
Switkes, M.
Yoon, J. U.

QUANTUM ELECTRONICS

A. Sanchez-Rubio, Leader
T. Y. Fan, Assistant Leader
T. H. Jeys, Senior Staff
J. J. Zayhowski, Senior Staff

Aggarwal, R. L.
Augst, S. J.
Chann, B.
Daneu, J. L.
Desmarais, L.
Goyal, A. K.
Herzog, W. D.

Hybl, J. D.
Le, X. T.
Lynch, E. J.
O'Brien, P. W.
Ochoa, J. R.
Ranka, J. K.
Ripin, D. J.

ELECTRO-OPTICAL MATERIALS AND DEVICES

J. C. Twichell, Leader
G. W. Turner, Assistant Leader
D. L. Spears, Senior Staff
C. A. Wang, Senior Staff
R. C. Williamson, Senior Staff

Bailey, R. J.
Calawa, D. R.
Calawa, S. D.
Connors, M. K.
Donnelly, J. P.
Duerr, E. K.
Goodhue, W. D.
Groves, S. H.
Hargreaves, J. J.
Harman, T. C.

Harris, C. T.
Huang, R. K.
Juodawlkis, P. W.
LaForge, B. E.
Liau, Z. L.
Mahan, J. M.
Mahoney, L. J.
Manfra, M. J.
McIntosh, K. A.
McNulty, D. D.

Missaggia, L. J.
Molnar, R. J.
Mull, D. E.
Napoleone, A.
Nitishin, P. M.
Oakley, D. C.
O'Donnell, F. J.
Plant, J. J.
Shiau, D. A.
Younger, R. D.

BIOSENSOR AND MOLECULAR TECHNOLOGIES

M. A. Hollis, Leader
T. H. Rider, Senior Staff

Blanchard, D. J.	Nargi, F. E.
Cabrera, C. R.	Parameswaran, L.
Graves, C. A.	Petrovick, M. S.
Harper, J. D.	Schmidt, T. L.
Lakdawala, S.	Schwoebel, E. D.
Mathews, R. H.	Zook, C. E.

ANALOG DEVICE TECHNOLOGY

M. A. Gouker, Leader
L. M. Johnson, Assistant Leader
A. C. Anderson, Senior Staff

Allen, M. S.	Oates, D. E.
Berggren, K. K.	Oliver, W. D.
Bolkhovsky, V.	Sage, J. P.
Fitch, G. L.	Santiago, D. D.
Ieni, S.	Seaver, M. M.
Lyons, W. G.	Slattery, R. L.
Macedo, E. M., Jr.	Weir, T. J.
Murphy, P. G.	

ADVANCED IMAGING TECHNOLOGY

B. B. Kosicki, Leader
R. K. Reich, Assistant Leader
B. E. Burke, Senior Staff

Aull, B. F.	Loomis, A. H.
Ciampi, J. S.	Mallen, R. D.
Cooper, M. J.	McGonagle, W. H.
Craig, D. M.	O'Mara, D. M.
Daniels, P. J.	Osgood, R. M.
Doherty, C. L., Jr.	Percival, K. A.
Dolat, V. S.	Rathman, D. D.
Felton, B. J.	Rose, M. K.
Gregory, J. A.	Stern, A.
Johnson, K. F.	Stevenson, C. N.
Lind, T. A.	Young, D. J.

ADVANCED SILICON TECHNOLOGY

C. L. Keast, Leader
V. Suntharalingam, Assistant Leader
P. W. Wyatt, Senior Staff

Austin, E. E.	Knecht, J. M.
Berger, R.	Lui, N. S.
Bozler, C. O.	Muldavin, J. B.
Brunelle, M. R.	Newcomb, K. L.
Burns, J. A.	Rabe, S.
Chen, C. K.	Soares, A. M.
Chen, C. L.	Travis, L.
D'Onofrio, R. P.	Tyrrell, B. M.
Fritze, M.	Warner, K.
Gouker, P. M.	Wheeler, B. D.
Healey, R. E.	Yost, D.-R.
Hu, W.	Young, G. R.

1. QUANTUM ELECTRONICS

1.1 DEVELOPMENT OF A UV LED-BASED BIOSENSOR

Biological weapons are a serious threat to our national security. The most deadly form of biological attack involves the aerosolization of agents and their subsequent inhalation and deposition in human lungs. Early detection of the presence of these agents is critical in defending against them.

Current biological agent point detection systems, as shown in Figure 1-1, are based on three components: the trigger, the collector, and the identifier. The trigger subsystem continuously monitors the ambient air for the presence of potential threat aerosols, and if such is present activates the collector and identifier subsystems, which then determine whether it actually contains the biological agents. Present collector and identifier subsystems are too expensive to operate continuously, and thus the main purpose of the trigger is to lower the overall operating cost of the biological detection system. The trigger must detect agent aerosols with high probability, while having a low false-trigger rate in environments of interest.

Two strategies for achieving high sensitivity and low false-trigger rate in a trigger subsystem are (1) development of high-sensitivity, high-discrimination detectors and (2) development of small, low-weight detectors that can be manufactured affordably in large numbers, spread over a wide area, as illustrated in Figure 1-2, and operated as part of a networked system. Generally, many elements contribute to the size, weight, and cost of a trigger detector. For a trigger technology based on sensing the light-induced fluorescence of biological agent particles in the air, one of the key factors is the light source.

DARPA has recently embarked on a program to develop semiconductor ultraviolet optical sources (SUVOS) that will operate down to wavelengths of 280 nm. Such light sources will be very small and

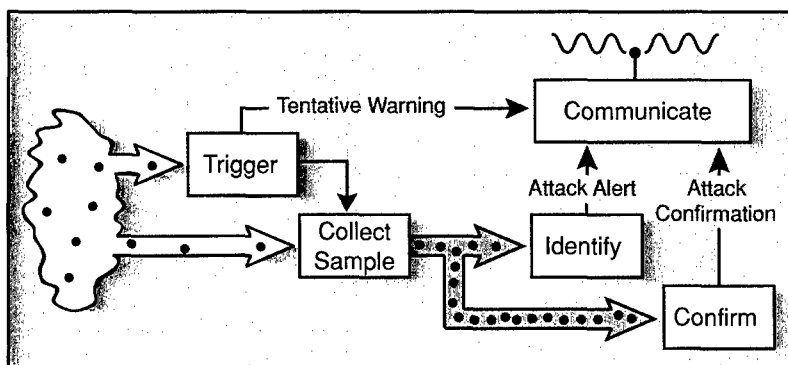


Figure 1-1. Schematic of generic biological agent detection system. The trigger must continuously operate and activate the sample collector whenever a threatening aerosol is present. The collector concentrates the aerosol particles, typically into a liquid, for presentation to the identifier. In the event of a positive identification a further confirmation identification procedure is performed.

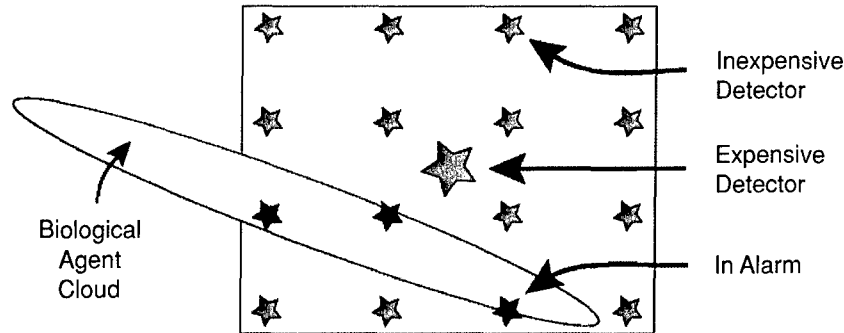


Figure 1-2. Illustration showing better protection by a large array of inexpensive detectors than by a single very high performance, expensive detector. For a point detector to sense a biological agent cloud, that cloud must pass over the detector; assuming some minimum level of detector performance a large array of detectors is more likely to be exposed to, and hence detect, a biological agent cloud than is a single detector.

inexpensive and should enable the development of small and low-cost biological agent trigger detectors. We are developing a biological agent sensor test bed for the purpose of using UV light-emitting diodes (LEDs) developed as part of the DARPA SUVOS program. This test bed will incorporate not only the SUVOS devices, but also novel photodetector and air sampling geometries that optimize the utility of the SUVOS devices for biological agent detection and that are also small and inexpensive.

The performance of a fluorescence-based biological agent detector depends on three considerations. First, enough UV radiation must be incident on the bioparticles to generate a measurable fluorescence signal. Second, the bioparticle optical signals must contain enough information for the detection algorithm to distinguish threat aerosols from common background aerosols. Third, the air sample rate must be large enough to detect enough threat particles in a sufficiently short time to accurately measure the threat concentrations of interest.

The detectable bioparticle concentration is given by

$$C = \frac{N_b}{\phi T} \quad (1.1)$$

where N_b is the number of bioparticles that must be detected in order to determine that the aerosol is threat-like, ϕ is the air sample rate, and T is the available sampling time. The number of photoelectrons detected from a biological particle as a result of light-induced fluorescence is given by

$$N_{pe} = \eta_d \sigma \frac{P}{Ah\nu} \tau \quad (1.2)$$

where η_d is the combined photo-signal collection and detection efficiency, σ is the bioparticle fluorescence cross section, P is the excitation light power, A is the cross-sectional area of the excitation light “beam,” $h\nu$ is the energy of an excitation photon, and τ is the time period during which the bioparticle is illuminated by the excitation light. The air sample rate is given by

$$\phi = \frac{AL}{\tau} \quad (1.3)$$

where L is the length of the excitation light beam over which particle signals can be detected.

Equations (1.1)–(1.3) can be combined to yield the minimum detectable concentration C in terms of the light source power P , the time T available to measure the concentration, the photon energy of the light source $h\nu$, the number of detected bioparticles N_b required to determine the concentration to a desired accuracy, the number of detected photoelectrons N_{pe} required to determine the presence of a bioparticle, the sample volume length L , the bioparticle fluorescence cross section σ , and the fluorescence detection efficiency η_d , as follows:

$$C = \frac{N_b}{L\sigma} \frac{N_{pe}}{\eta_d} \frac{h\nu}{PT} \quad (1.4)$$

One of the most important variables in Equation (1.4) is the fluorescence cross section σ of the biological agent [1]–[3]. This cross section can vary over a large range depending on the particle size and particle composition. Representative cross sections are shown in Table 1-1, and these were used to generate the plots in Figure 1-3.

Equation (1.4) and Figure 1-3 allow a quick assessment of the biological agent detection sensitivity that can be achieved for a given excitation light power. Not shown in this analysis is the effect of the LED emitting area on the sample volume and on the transit time of the bioparticle through this sample volume. In general, for a given light output power, a smaller LED emitting area will allow the design of a smaller biodetector. Since the development of a small biological agent sensor is a major goal of our program, we desire bright LEDs, i.e., high power from a small emitting area.

A schematic of a UV LED-based biological agent trigger is shown in Figure 1-4. Air is drawn through a nozzle (top) and into a sample volume illuminated by both 280- and 340-nm light from different LEDs. The LED light is re-imaged by elliptical mirrors into the sample volume with ~50% collection efficiency. Biological agent particles in the airstream pass through the sample volume and are illuminated by the LED light. The particles both elastically scatter the incident light and emit fluorescence induced by the incident light. The scattered light and fluorescent light are collected and imaged into a fiberoptic bundle by a third elliptical mirror. The light entering the fiber-optic bundle is distributed to four photodetectors. The photodetectors measure the amount of 280- and 340-nm elastic scattering, the amount of 340- and 450-nm fluorescence induced by the 280-nm LED light, and the amount of 450-nm fluorescence induced

TABLE 1-1
Description of Variables Used in Equation (1.4) and the
Values Assumed for These Variables in Figure 1-3

Variable	Symbol	Value Assumed in Figure 1-3
Minimum Detectable Concentration	C	--
Number of Detected Bioparticles	N_b	100
Effective Length of Light Beam	L	1 cm
Bioparticle Fluorescence Cross Section	σ	$(150, 22, 2.6) \times 10^{-12} \text{ cm}^2$ (290, 340, 400 nm)
Number of Detected Photoelectrons	N_{pe}	100
Photocollection and Detection Efficiency	η_d	0.2%
Light Source Photon Energy	$h\nu$	$(6.8, 5.8, 5.0) \times 10^{-19} \text{ J}$ (290, 340, 400 nm)
Excitation Light Power	P	--
Threat Detection Time	T	100 s

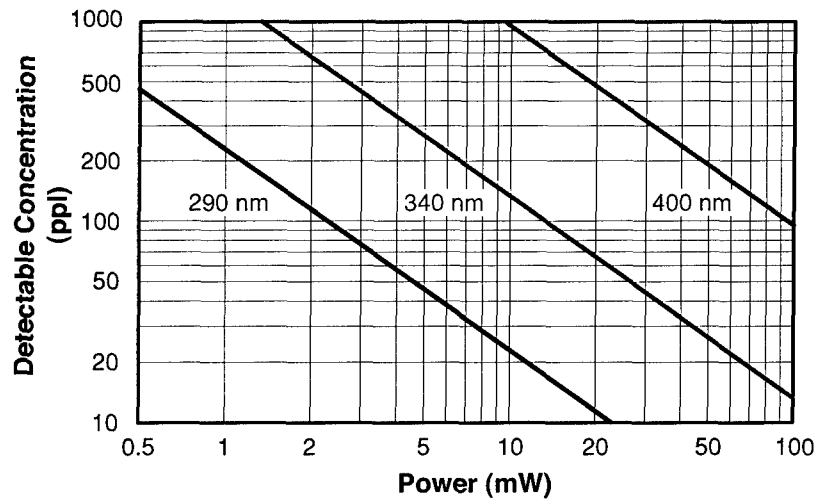


Figure 1-3. Minimum detectable concentration as a function of average optical power for bioparticle cross sections at fluorescence excitation wavelengths of 290, 340, and 400 nm. See Equation (1.4) and Table 1-1.

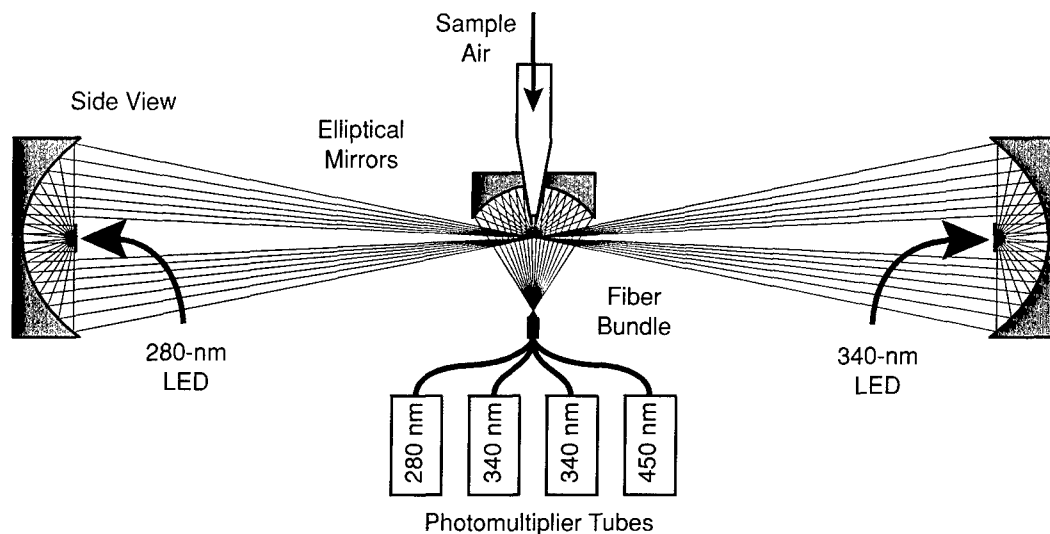


Figure 1-4. Schematic for UV light-emitting diode based biological agent sensor trigger.

by the 340-nm LED light. To avoid confusion of elastic scattering and fluorescence signals, the LEDs are alternately pulsed at a 50% duty cycle. In addition, the 340-nm fluorescence detector is turned off whenever the 340-nm LED is on, to avoid possible damage to this detector. In this design, the LED emitting diameter is taken to be 0.25 mm, and the distance from one LED elliptical mirror to the other is 80 mm.

The experimental apparatus used for measuring the elastic scattering and fluorescence signals of single bacterial spores of *Bacillus globigii* is shown in Figure 1-5. An aerosol of the bacterial spores was passed through the sample volume (10^{-9} liter) of the collection mirror. The concentration of the spores was low enough that at most one spore was resident in the sample volume at any time. In order to test this apparatus without the additional complication of utilizing low-brightness LEDs, which we do plan to incorporate later, we began testing with a 408-nm laser diode [4]. The spores were illuminated by light from a 408-nm laser diode with an average power of 3.5 mW. This light was focused to a spot size of 0.35×0.55 mm at the focus of the signal collection elliptical mirror. The elastic scattering and fluorescence from a given spore were reflected by the collection mirror to a fiber optic that was mated to a Perkin Elmer MH1343 microchannel photomultiplier tube. At high gain this photomultiplier tube has a pulse height distribution that easily resolves single photon signals from low-amplitude noise. At a fixed illumination of this tube, it is possible to measure the charge per photocathode photoelectron at high gain and then to extrapolate the average charge per photoelectron to lower gains.

The elastic scattering and fluorescence oscilloscope traces shown in Figure 1-5 were taken with the photomultiplier operating at a gain that generated on average 1 pC of anode charge for every photocathode

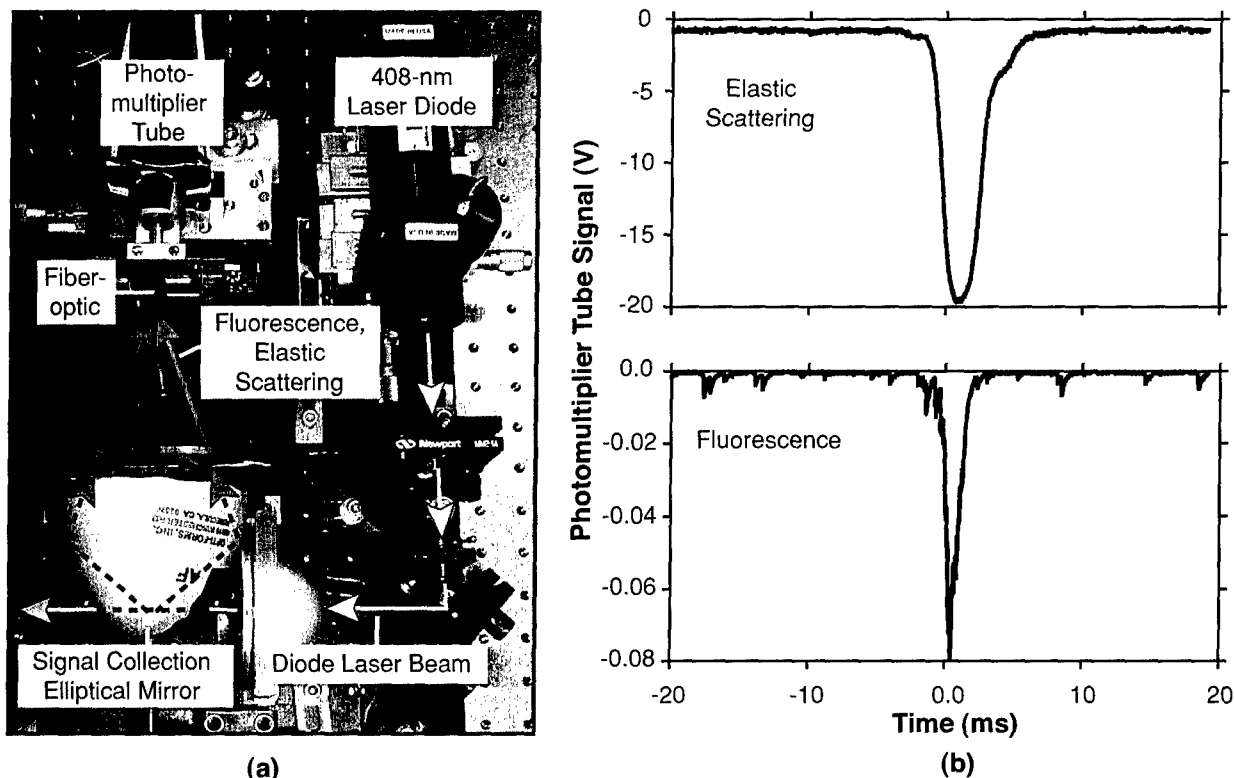


Figure 1-5. (a) Photograph of experimental apparatus for measuring biological particle signals utilizing a laser diode light source, and (b) oscilloscope traces of elastic scattering and fluorescence signals from single *Bacillus globigii* spores.

photoelectron. The traces were recorded by a digital oscilloscope operating with 1-M Ω input impedance and 13-pF input capacitance. The elastic scattering signal was obtained by allowing all of the collected radiation to pass to the photomultiplier, while the fluorescence signal was obtained by passing the collected radiation through a 2-mm-thick Schott glass GG435 filter before passing to the photomultiplier. The GG435 filter absorbs all of the elastically scattered 408-nm radiation while passing a large fraction of the fluorescence radiation. The elastic scattering signal corresponds to the detection of about 40,000 photocathode photoelectrons, and the fluorescence signal corresponds to the detection of about 80 photocathode photoelectrons. These signal levels correspond roughly to an elastic scattering cross section equal to the geometric cross section of a single bacterial spore and a fluorescence cross section (at 400 nm) as given in Table 1-1.

Thus, a biological agent sensor test bed is being developed that will utilize semiconductor UV optical sources (specifically LEDs) developed as part of the DARPA SUVOS program. We have demonstrated that a low-power laser diode source (408 nm) can generate detectable elastic scattering and

fluorescence signals from single bacterial spores. Moreover, the magnitude of the signals is consistent with the expected elastic scattering and fluorescence cross sections.

T. H. Jeys	L. Desmarais
E. J. Lynch	J. R. Ochoa

REFERENCES

1. G. W. Faris, R. A. Copeland, K. Mortelmans, and B. V. Bronk, *Appl. Opt.* **36**, 958 (1997).
2. S. D. Christesen and K. K. Ong, Edgewood Research Development and Engineering Center US CBDCOM Report No. ERDEC-TR-466, 1998.
3. P. J. Hargis, Jr., P. J. Brannon, C. H. Ching, et al., Edgewood Chemical Biological Center SBCCOM Report No. ECBC-CR-028, 2000. (DTIC ADB257794)
4. J. Ho, P. Hairston, and M. Spence, Defense R&D Canada Technical Report No. RES TR 2000-190, July 2001.

2. ELECTRO-OPTICAL MATERIALS AND DEVICES

2.1 WAFER FUSION OF GaSb TO GaAs

GaSb-based III-V semiconductors are of significant interest for high-speed, low-power electronics and mid-infrared optoelectronics. The performance and functionality of these devices could be improved if the epilayer structures were grown on a semi-insulating (SI) GaSb substrate [1]–[8]. However, since these substrates are not available, a variety of alternative approaches such as growth on specially designed buffer layers [1]–[2],[7], GaSb transfer by hydrogen implantation [3]–[4], lateral epitaxial overgrowth [5], and wafer bonding with intermediate layers [6],[8] have been pursued. Atomic fusion by covalent bond formation is a promising approach for monolithic integration and has been successfully demonstrated for GaAs, InP, and GaP wafers [9]–[12]. These As- and P-based materials have a significant dissociation vapor pressure, and atomic fusion occurs by mass transport [9]. GaSb, however, has a relatively low melting point of 712°C and a considerably lower vapor pressure compared to the As- and P-based alloys. Therefore, GaSb wafer fusion may be quite different and more difficult. Here, we report wafer fusion of GaSb to SI GaAs. Fusion to SI GaAs was selected since its thermal expansion coefficient α is more closely matched to GaSb than InP: $\alpha(\text{GaSb}) = 6.9 \times 10^{-6} \text{ K}^{-1}$, $\alpha(\text{GaAs}) = 5.7 \times 10^{-6} \text{ K}^{-1}$, $\alpha(\text{InP}) = 4.6 \times 10^{-6} \text{ K}^{-1}$.

Wafer fusion was initially studied by using commercially available polished GaSb and SI GaAs wafers, since the success of wafer fusion can be limited by surface roughness, defects, contamination, and wafer bow. The mirror-smooth GaAs wafer was first coated with pyrolytic silicon dioxide, and then mechanically lapped to a thickness $<200 \text{ }\mu\text{m}$ to aid in surface-tension pulling, as discussed below. In addition, in some fusion experiments the GaAs wafer was first patterned with a periodic pattern of grooves. The grooves, which were photolithographically defined and chemically etched, were typically $1 \text{ }\mu\text{m}$ deep and $25 \text{ }\mu\text{m}$ wide with periodicity of $250 \text{ }\mu\text{m}$. Both wafers were then cleaved into $1 \times 1\text{-cm}$ pieces. To prepare for fusion, GaSb and GaAs wafers were successively cleaned ultrasonically in trichlorethylene, acetone, and methanol; etched in HCl and diluted HF, respectively, in order to remove oxides; and rinsed in methanol. The surfaces of the wet wafers were then placed in contact with one another to allow liquid-surface tension to pull the wafers into atomic contact [13]. The Van der Waals-bonded wafers were then enclosed in a quartz capsule along with additional GaSb and GaAs wafers as a vapor source, unless stated otherwise. The wafers were atomically fused by heat treatment of the samples at temperatures ranging from 475 to 576°C and times from 100 to 160 h, with the vapor source either held at higher temperatures or used as cover wafers. In these experiments, no mechanical pressure, which can induce defects, was applied during the heat treatment.

Fusion of GaSb-based epitaxial layers to SI GaAs was accomplished in a similar manner, except that the fusion temperature was reduced to 350–480°C, since a lower temperature would result in reduced residual stress, which is more desirable for device structures. Since there were growth defects on epitaxial layers, in some cases mechanical pressure was applied to ensure surface-to-surface contact using a specially designed quartz/graphite holder [9]. Heat treatment times ranged from as short as 50–120 h. The epitaxial layer structure, which is of interest for lattice-matched thermophotovoltaics, was grown lattice

matched to a GaSb substrate and consisted of the following layers: 0.1- μm GaSb buffer layer, 0.5- μm InAsSb etch stop layer, 0.1- μm GaSb confining layer, 1- μm GaInAsSb active layer, and 0.1- μm GaSb confining layer. The layers were grown by organometallic vapor phase epitaxy, as described elsewhere [14].

The fusion of the epitaxial layer to the GaAs wafer was followed by chemical removal of the GaSb substrate, GaSb buffer layer, and InAsSb etch stop layer [8]. The bulk of the substrate was first etched in tartaric: H_2O_2 :HF: H_2O . The remaining GaSb substrate and GaSb buffer layer were selectively etched using CrO_3 :HF: H_2O until the InAsSb layer was exposed. Finally, the InAsSb etch stop layer was removed with H_2O_2 saturated with citric acid.

Figure 2-1 shows a scanning electron microscope (SEM) image of a cleaved cross section of GaAs and GaSb wafers fused without pressure at 576°C for 140 h. The interface between the wafers is identified by the presence of voids, which result from mass transport surface energy minimization (i.e., condensation of the thin gaps) [9]. The voids varied in width from a few to several hundreds of nanometers, and were typically less than about 20 nm high. Since the gaps between the physically bonded wafers are initially very thin, the range of the void height is smaller compared to the width. The density of the voids decreased with increased temperature. This observation is consistent with the coalescence of voids by mass transport.

GaSb and GaAs wafers were annealed at a lower temperature of 500°C for 140 h. The surface of the GaAs wafer in one set of wafers was the mirror-polished finish, while the surface of the GaAs in another set had the etched grooves. The wafers in the set without the grooved GaAs surface separated upon cleaving. However, the wafers in the other set with the grooved GaAs remained intact upon cleaving. Therefore, atomic fusion appears enhanced by using GaAs wafers that have a grooved surface pattern. In another experiment, GaSb and groove-patterned GaAs wafers were annealed at 475°C for 120 h with and without an As and Sb overpressure. The wafers with the overpressure were fused, while those without the overpressure separated upon cleaving. Thus, wafer fusion is improved by patterning the surface as well as by providing an increased overpressure of As and Sb atomic species at the GaSb/GaAs interface. The

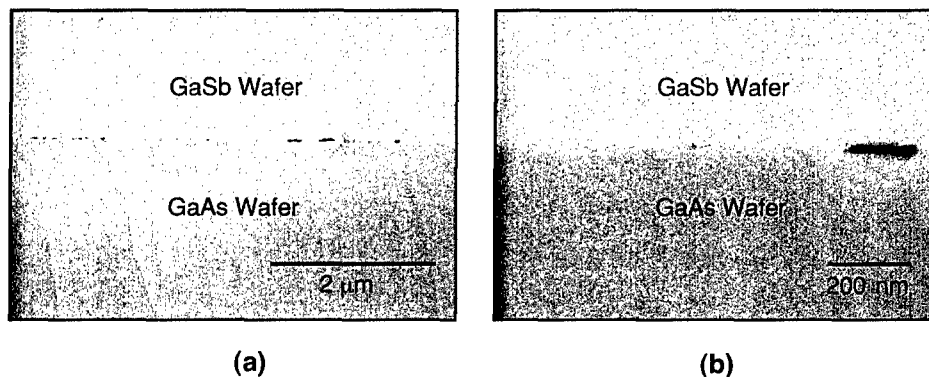


Figure 2-1. Scanning electron micrograph (SEM) of cleaved cross section of GaSb and GaAs wafers fused without pressure at 576°C for 140 h at (a) low magnification and (b) high magnification.

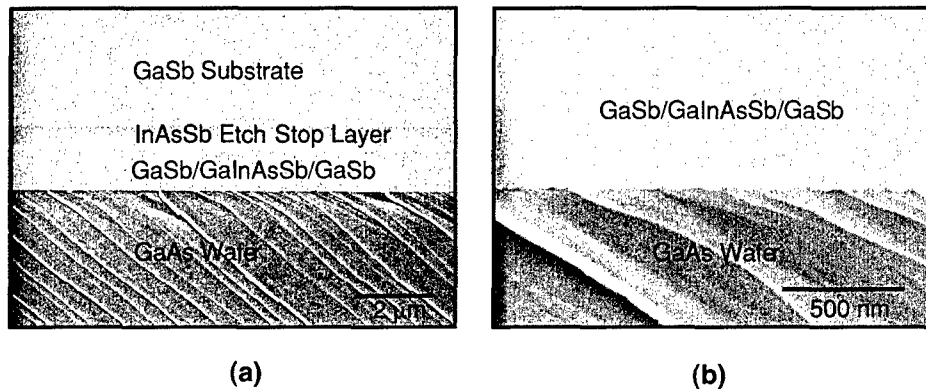


Figure 2-2. SEMs of cleaved cross section of lattice-matched GaSb/GaInAsSb/InAsSb/GaSb heterostructure fused to GaAs at 400°C for 53 h with pressure: (a) full image of GaSb/GaInAsSb/InAsSb heterostructure, GaSb substrate, and GaAs wafer; and (b) enlarged view of fused interface.

grooves can assist surface-tension pulling by providing more pulling points. In addition, the grooves provide channels to supply an overpressure of As and Sb atomic species, thus promoting mass transport and atomic fusion.

GaSb/GaInAsSb/InAsSb/GaSb lattice-matched heterostructures and GaAs wafers were fused at lower temperatures of 350–480°C for reduced thermal stress. The surface of the GaAs wafer was either mirror polished or etched with grooves. Since experiments with GaSb and GaAs wafers described above indicated that GaAs wafers without grooves were not fused when annealed at temperatures of 500°C, pressure was applied to those samples that did not have grooves. In addition, pressure is advantageous since the surface of epitaxial layers exhibited growth defects. It was found that epilayers could be fused to GaAs with annealing temperatures as low as 350°C and with As and Sb overpressure, both without pressure for the grooved GaAs and with pressure for mirror-polished GaAs. The application of pressure during fusion decreased void formation, as would be expected. Figure 2-2 shows a cleaved cross section of a GaSb/GaInAsSb/InAsSb/GaSb heterostructure fused to a GaAs wafer at 400°C for 53 h with pressure. In this sample, the void height was typically <10 nm.

The epitaxial transfer of GaSb/GaInAsSb/GaSb to GaAs was completed by selective removal of the GaSb substrate and the InAsSb etch stop layer. Figure 2-3 shows the high-resolution x-ray diffraction rocking curves for GaSb/GaInAsSb/GaSb fused with and without pressure, respectively, at 400°C. The diffraction peak of the sample fused with pressure, shown in Figure 2-3(a), is extremely broadened with full width at half-maximum (FWHM) of 335 arc s. A much narrower FWHM value is obtained for the sample fused without pressure, shown in Figure 2-3(b), with FWHM of 66 arc s. In addition, observation of thickness fringes in the sample shown in Figure 2-2(b) is indicative of minimal residual stress. The FWHM value is somewhat larger than that measured for GaInAsSb/GaSb epilayers that were not bonded (FWHM ~30 arc s). Reciprocal space mapping revealed that the broadening is due to layer tilt, which is

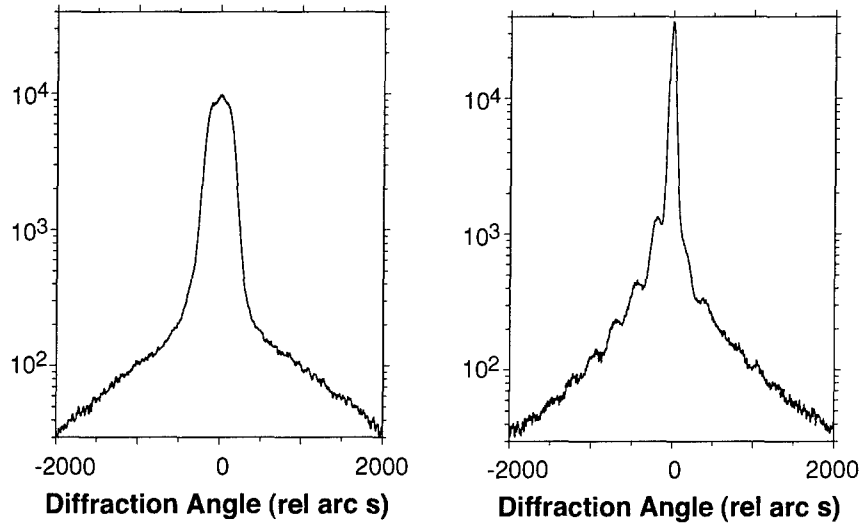


Figure 2-3. X-ray diffraction of GaSb/GaInAsSb/GaSb heterostructure fused (a) to a smooth GaAs wafer with pressure and (b) to a grooved GaAs wafer without pressure.

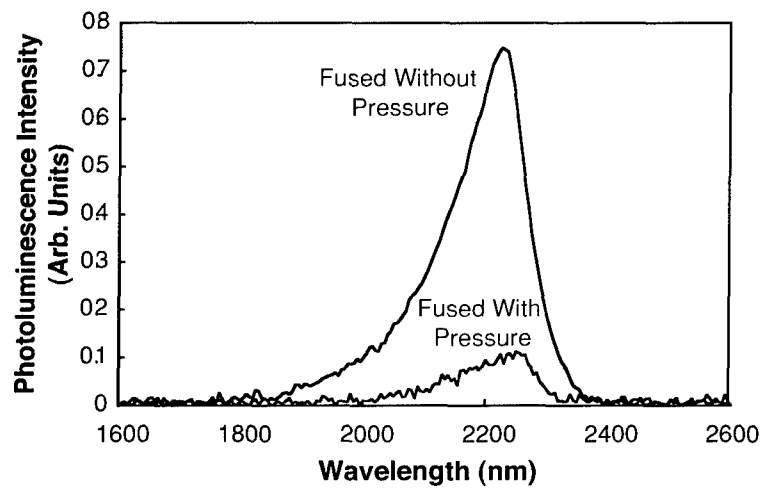


Figure 2-4. 300-K photoluminescence of GaSb/GaInAsSb/GaSb heterostructures fused to GaAs with and without pressure.

likely due to wafer curvature for the sample fused without pressure. The broadening for the sample fused with pressure is probably due to wafer curvature as well as stress-induced defects that result from pressure during annealing. The FWHM value of the sample fused at 350°C with pressure is slightly smaller at 283 arc s.

Good luminescence efficiency is important for optoelectronic devices, and Figure 2-4 shows a comparison of 300-K photoluminescence (PL) spectra for GaSb/GaInAsSb/GaSb fused with and without pressure at 400°C. The sample fused without pressure utilized a grooved GaAs wafer. The PL peak intensity is approximately 7 times greater for the sample fused without pressure. These results suggest that the application of mechanical pressure introduces crystal defects, as might be expected, and the defect generation is associated with nonradiative recombination centers. Compared to the sample fused with pressure, the PL intensity of another sample fused at a lower temperature of 350°C with pressure is higher by about a factor of 3.

GaSb/GaInAsSb/GaSb epitaxial layers were fused to SI GaAs wafers at temperatures as low as 350°C and without application of mechanical pressure. A periodically grooved GaAs surface and an overpressure of As and Sb atomic species at the GaAs/GaSb interface aid in promoting mass transport and atomic fusion. The structural and optical properties are significantly better for samples that are fused without pressure. These results suggest that wafer fusion of GaSb and GaAs is very promising for monolithic device integration and other applications that require the use of an electrically insulating substrate.

C. A. Wang	Z. L. Liao
P. M. Nitishin	D. A. Shiao
D. R. Calawa	J. W. Chludzinski
J. M. Porter	

REFERENCES

1. H.-R. Blank, M. Thomas, K. C. Wong, and H. Kroemer, *Appl. Phys. Lett.* **69**, 2080 (1996).
2. K. G. Eyink, M. L. Seaford, T. W. Haas, D. H. Tomich, W. V. Lampert, S. D. Walck, J. S. Solomon, W. C. Mitchel, and L. F. Eastman, *J. Vac. Sci. Technol. B* **15**, 1187 (1997).
3. K. D. Hobart and F. J. Kub, *Electron. Lett.* **35**, 675 (1999).
4. Y. Zheng, P. D. Moran, Z. F. Guan, S. S. Lau, D. M. Hansen, T. F. Kuech, T. E. Haynes, T. Hoechbauer, and M. Natasi, *J. Electron. Mater.* **29**, 916 (2000).
5. S. S. Yi, D. M. Hansen, C. K. Inoki, D. L. Harris, T. S. Kuan, and T. F. Kuech, *Appl. Phys. Lett.* **77**, 842 (2000).
6. P. D. Moran, D. Chow, A. Hunter, and T. F. Kuech, *Appl. Phys. Lett.* **78**, 2232 (2001).

7. M. N. Palmisiano, R. M. Biefeld, J. G. Cederberg, M. J. Hafich, and G. M. Peake, *AIP Conf. Proc.* **653**, 305 (2003).
8. C. A. Wang, P. G. Murphy, P. W. O'Brien, D. A. Shiau, A. C. Anderson, Z. L. Liao, D. M. DePoy, and G. Nichols, *AIP Conf. Proc.* **653**, 473 (2003).
9. Z. L. Liao and D. E. Mull, *Appl. Phys. Lett.* **56**, 737 (1990).
10. Y. H. Lo, R. Bhat, D. M. Huang, M. A. Koza, and T. P. Lee, *Appl. Phys. Lett.* **58**, 1961 (1991).
11. J. J. Dudley, D. I. Babic, R. Mirin, L. Yang, B. I. Miller, R. J. Ram, T. Reynolds, E. L. Hu, and J. E. Bowers, *Appl. Phys. Lett.* **64**, 1463 (1994).
12. F. A. Kish, F. M. Steranka, D. C. DeFevere, D. A. Vanderwater, K. G. Park, C. P. Kuo, T. D. Osentowski, M. J. Peanasky, J. G. Yu, R. M. Fletcher, D. A. Steigerwald, M. G. Craford, and V. M. Robbins, *Appl. Phys. Lett.* **64**, 2839 (1994).
13. Z. L. Liao, *Appl. Phys. Lett.* **77**, 651 (2000).
14. C. A. Wang, H. K. Choi, and G. W. Charache, *IEE Proc.-Optoelectron.* **147**, 193 (2000).

3. SUBMICROMETER TECHNOLOGY

3.1 FABRICATION OF DAST ELECTRO-OPTIC WAVEGUIDES USING GRAPHOEPIITAXIAL CRYSTAL GROWTH

The development of organic electro-active materials that could be used for optical modulators has generated considerable interest. These materials must be compatible with a variety of substrates and processing techniques, and they offer a large electro-optic coefficient leading to efficient modulators. In addition, the optical and rf properties of these materials should be well suited to wideband (>100 GHz), traveling wave modulator implementations. One material, 4-dimethylamino-N-methyl-4-stilbazolium tosylate (DAST), is particularly interesting because it forms an organic crystalline structure with an exceptionally large electro-optic coefficient.

The use of DAST has been limited by the difficulty of obtaining device-quality crystals of the proper dimensions. Graphoepitaxy [1]–[3], which utilizes lithographically defined structures to modify crystal growth, has demonstrated control of crystal growth and orientation [4]–[6]. Here, we demonstrate the use of this technique to obtain device-quality crystals of DAST, while increasing crystal growth rate by orders of magnitude. Rapid growth rates are important for organic materials like DAST that decompose at their melting temperature. Growth rates of DAST from graphoepitaxially controlled melts are $1\text{--}2\text{ mm s}^{-1}$, $\sim 10^5$ faster than by a solution growth technique [7]–[9].

DAST is known to thermally decompose above its melting temperature, 259°C . However, the decomposition rate is not linear with time, as shown in Figure 3-1. Like many other organic materials, the decomposition rate is proportional to the time-dependent concentration of radicals [10]. The sudden

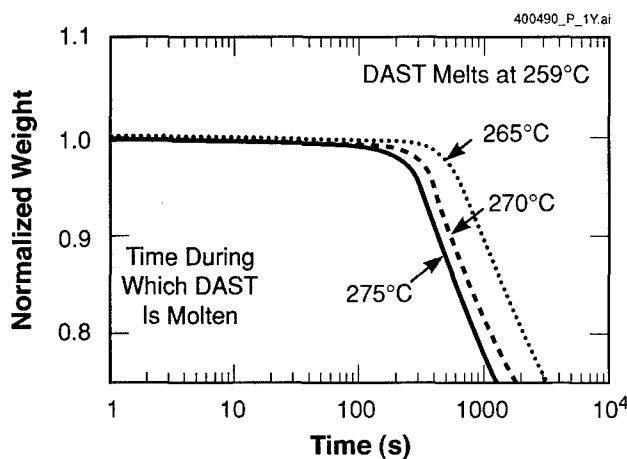


Figure 3-1. Weight of molten DAST in flowing dry nitrogen as a function of time for several temperatures. It is assumed that the weight loss is directly related to decomposition.

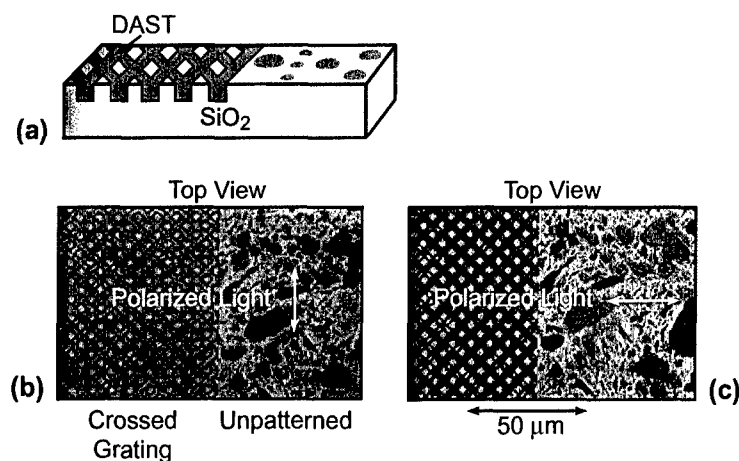


Figure 3-2. DAST melted and solidified on SiO₂. (a) Schematic diagram showing the cross section of a substrate with the grating on the left and the unpatterned surface on the right. (b) Optical micrograph of DAST using polarized light as indicated. (c) Optical micrograph of the same region shown in (b) but with the illuminating polarization changed. Note the random orientation of the crystallites on the unpatterned surface and the consistent orientation in the grating region.

increase in the rate of weight loss of molten DAST for times greater than 200–500 s may be due to the time required for the generation of a critical concentration of radicals. If DAST can be melted and resolidified sufficiently fast before significant radicals can form, then device-quality crystals can be obtained.

The graphoeptaxy technique was used to control the solidification and orientation of the DAST crystals. Silicon wafers were over-coated with 5–10 μm of chemically vapor deposited (CVD) SiO₂. Crossed gratings with periods from 2 to 12 μm intersecting at ~95° to match the natural crystalline facet of DAST were etched 0.5–1 μm deep into the SiO₂. A DAST-water-methanol-glycerin paste was deposited, pressing it into the etched structures with sufficient shearing force that the red crystals became green. The DAST-coated substrate was placed on a strip heater [11] in flowing dry nitrogen and heated to the melting point of DAST in 1–2 min. At about 150°C the water, methanol, and glycerin evaporated causing the green mass to turn dark red. When the occurrence of melting was clearly visible, the heater power was reduced by ~50% and the DAST resolidified over 20 s. A thermal gradient built into the oven allowed for directional solidification forming crystals 1–5 mm wide and 5–15 mm long.

Figure 3-2 shows the effect of the crossed gratings on crystal growth. Without the gratings the molten DAST beads into individual droplets that super cool and quickly solidify to form heavily defective

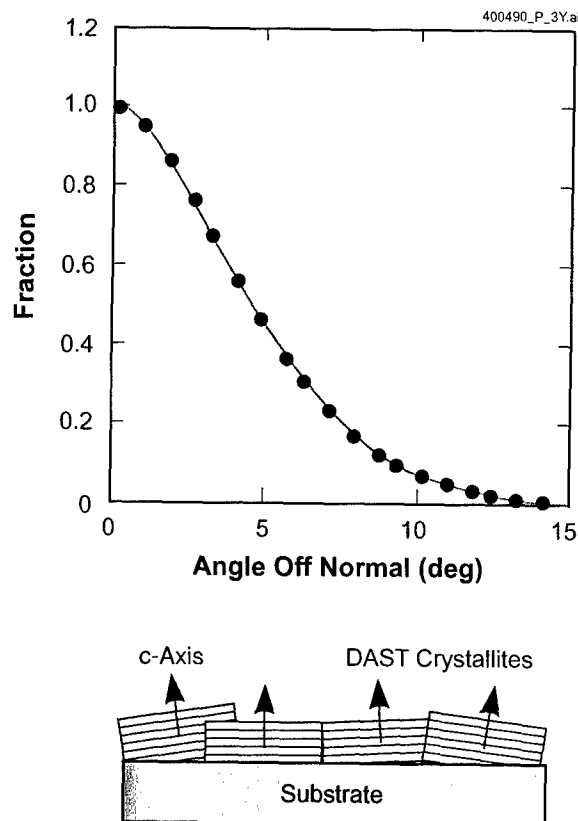


Figure 3-3. Distribution of *c*-axis of crystallites as a function of angle from the substrate normal. Half of the DAST crystalline volume has its *c*-axis less than 4.5° from substrate normal and 90% is within 9° . The inset shows a schematic diagram of crystallites with their *c*-axis a few degrees from the substrate normal.

crystals of random orientation. In the grating the molten mass remains in the etched regions as a contiguous film, which solidifies from regions not fully melted. X-ray analysis indicates that for the resolidified DAST the *c*-axis is normal to the substrate to within approximately $\pm 4^\circ$, as shown in Figure 3-3.

DAST waveguides were obtained by etching in the SiO_2 substrate and using the crystals growing on the crossed gratings to seed molten DAST in the waveguide forms. The gratings were previously coated with ~ 100 nm of conductive TiN, Cr, or Al, which was used as an electrical contact to the waveguides, as shown in Figure 3-4. Not all the waveguides have the *a*-axis normal to the axis of the waveguide, as is desirable for maximum optical-electrical interaction. Thus, after growth the substrate is cleaved to isolate the crystals with the desired properties. The Si wafer supporting the SiO_2 -DAST structure breaks along the (110) planes, so flat cleaves normal to the waveguide axis are straightforward.

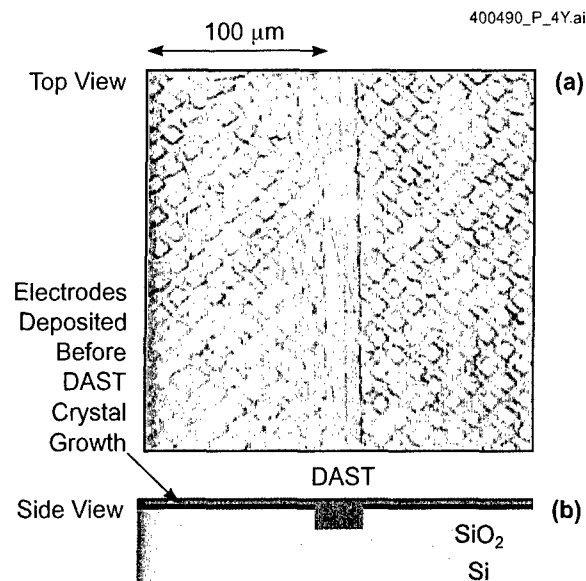


Figure 3-4. (a) Optical micrograph of DAST waveguide 4 μm deep and 15 μm wide, which was seeded from crystals on either side. The crossed gratings were over-coated with 100 nm of Cr before DAST deposition and used to electrically contact the crystal. (b) Schematic cross section of substrate shown in (a). The lower Si substrate is used to give a well-defined cleaving plane normal to the waveguides.

The waveguides, 2–15 μm wide and 2–4 μm deep, are not single mode. However, by applying an electric field to the electrodes on the SiO_2 substrate, optical modulation has been demonstrated. DAST Mach-Zehnders exhibited $V_\pi L$ from 7.5 to 16.5 V mm and the calculated dn/dE is $600 \pm 300 \text{ pm V}^{-1}$, which is an order of magnitude greater than that of LiNbO_3 . Waveguides without electrodes had optical losses $< 10 \text{ dB cm}^{-1}$.

The success of graphoepitaxy with DAST is the result of three effects. DAST crystals have a large anisotropy and tend to grow from the melt with their c-axis normal to the plane of the substrate. The crossed gratings stabilize the molten DAST film, allowing for seeding, and the rapid crystal growth minimizes decomposition. If the material remains molten for more than a minute, the resolidified material appears amorphous and does not interact with polarized light, indicating that it does not have a large electro-optic coefficient.

M. W. Geis	M. F. Marchant
R. Sinta	K. E. Krohn
W. Mowers	S. J. Spector
S. J. Deneault	D. R. Calawa
T. M. Lyszczarz	

3.2 ANGLE-RESOLVED SCATTERING MEASUREMENT SYSTEM FOR 157-nm OPTICS

As the semiconductor industry transitions to 157 nm, the impact of flare on imaging performance is expected to become more severe than at 248 and 193 nm. From simple scaling laws, Lai et al. [12] estimate that flare is expected to increase by a factor of 2.5 at 157 nm compared to 248 nm. In general, flare levels are evaluated lithographically on the exposure tool or calculated indirectly through modeling from surface roughness data collected with atomic force microscopy (AFM) or optical interferometry [12]–[14]. In contrast, we have designed and implemented a system that directly measures angle-resolved scattering (ARS) at 157 nm. This system allows scattered light to be measured element by element at the exposure wavelength, allowing optimization of substrate polishing and thin film coating conditions to be performed before final system integration.

The system we have developed measures stray light from a F_2 laser to within $\sim 4^\circ$ from the specularly transmitted beam, sensing intensity changes of over 7 orders of magnitude. The scattered light over this angular range corresponds to light scattered from components of surface roughness with spatial wavelengths $< 2 \mu\text{m}$. Better angular resolution, corresponding to larger spatial wavelengths, can be obtained with this system at the expense of reducing the dynamic range of the detected signal.

A schematic drawing of the ARS test bed is shown in Figure 3-5. A quasi-coherent source is produced by a combination of two spatial filters. The first filter comprises two 1-mm apertures spaced 1 m apart, limiting the divergence of the laser beam to ~ 1 mrad. The second filter is a precision machined $100\text{-}\mu\text{m}$ pinhole in a $25\text{-}\mu\text{m}$ -thick tungsten membrane placed at the focus of a 150-mm CaF_2 singlet lens. The combination of two spatial filters was found necessary to produce a circularly symmetric diffraction pattern at the lens when using a 4-W F_2 laser (Lambda Physik LPF200). A 416.9-mm focal length singlet CaF_2 lens images the pinhole. The lens is placed at a distance ~ 10 times further from the detector than the sample. This arrangement is used to limit the contribution of scatter from the lens compared to that from the test sample, since scattering falls off quadratically with distance. Ray tracing was used to confirm that secondary reflections between the lens surfaces did not reconverge in the image field. From the analysis, rays from secondary reflections were found to image at a point 67 mm from the lens. By using a simple aerial image simulator, it is predicted that the rapidly diverging rays do not contribute significantly to the background signature. Ray tracing is also used to confirm that back reflections off the detector housing do not impact the background signature. In order to minimize scatter by the optics housing of the specularly transmitted beam, the beam is allowed to exit the box and dissipate in air.

Scattered light is measured with a photomultiplier tube (PMT) (Perkin Elmer channel model 910) biased to 1500 V and mounted on a goniometer. The total pulse energies are measured by integrating the photoinduced charge generated by the PMT through a 10-pF capacitor. The signal is buffered by a junction field-effect transistor (JFET) op-amp and fed directly into a Joulemeter (Molelectron model OM4000). A $330\text{-k}\Omega$ bypass resistor is used to dissipate the capacitor charge between pulses. The PMT uses a CsI photocathode and is solar blind above 230 nm. Using a glass plate absorptive at 157 nm over the detector, we confirmed that contributions of the small red component (~ 720 nm) of the F_2 beam were not amplified. In addition, from simple estimates, fluorescence in CaF_2 , which generally occurs above 287 nm [15], can be neglected.

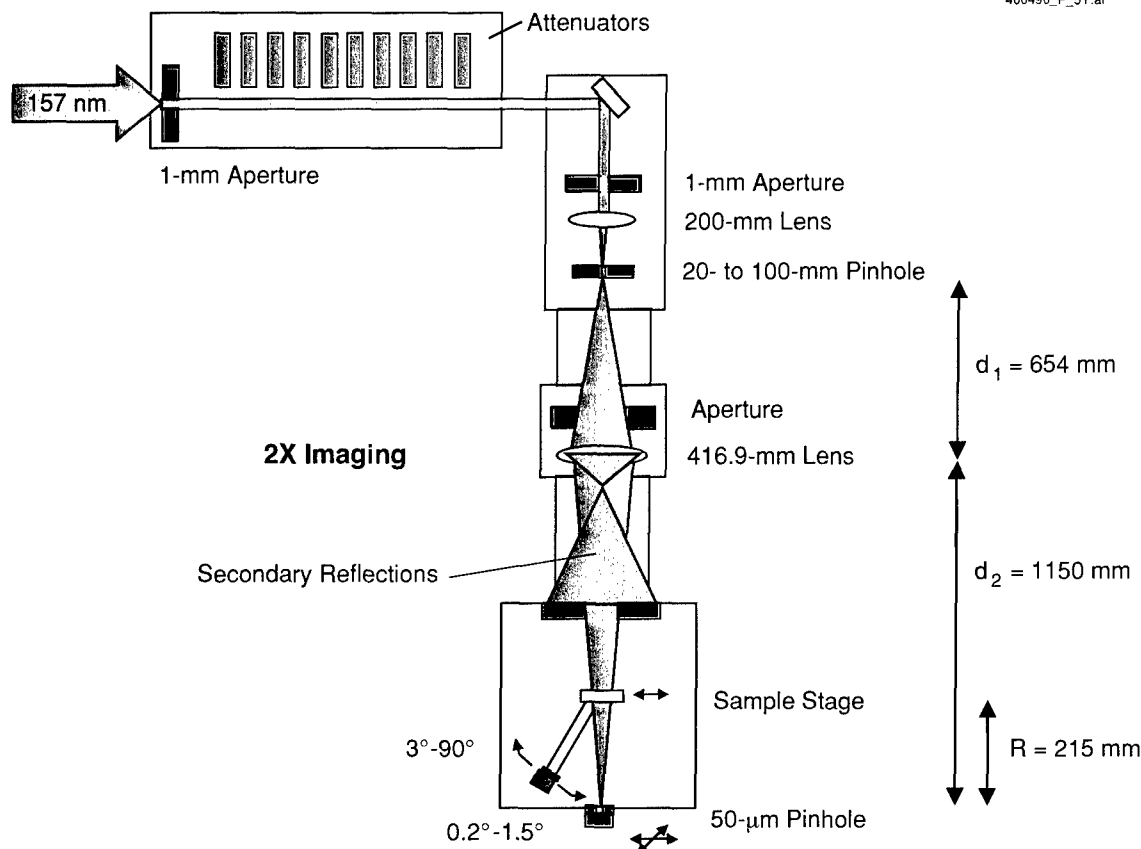


Figure 3-5. Schematic drawing of 157-nm angle-resolved scattering measurement system. A $2\times$ magnification system is used to image a coherently illuminated pinhole. Two separate detectors are employed for small- and large-angle scattering measurements. The entire beam path is purged with nitrogen.

In performing the ARS measurements, intensity levels are compared with the sample in and out of the beam line as the detector is rotated through the specular beam. Levels measured with the sample in the beam line above the background signature are attributed to scattered light generated from the sample. The diameter of the pinhole, pupil function of the system and the aperture size of the detector determine the resolution of the instrument at angles near the specular beam. In the simple imaging system employed, the roll-off of the aerial image is extremely sensitive to the diameter of the entrance window of the imaging optic. Figure 3-6 shows aerial image simulations of the expected beam profile for three different radii of the entrance window. The maximum drop-off occurs when the radius of the aperture equals 1.25 mm, the radius of the primary lobe of the diffracted beam emanating from the pinhole. The inset graph plots the intensity at 0.5° from the specular beam as the aperture radius is varied. Changes of only a few percent alter the background intensity at this angle by almost 2 orders of magnitude. In practice, we were unable to

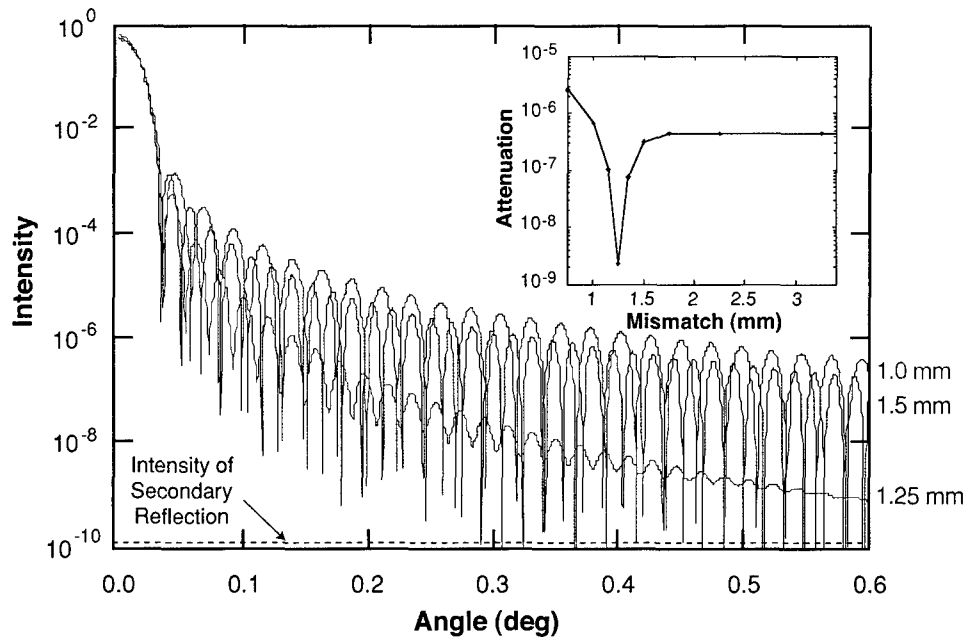


Figure 3-6. Simulated aerial image for three different radii of the entrance window using a 100- μm pinhole in the object plane. A semi-analytic scalar field propagation model was used to predict the aerial image. The scalar field at a given reference plane is first discretized. The resulting field at a new position along the optic axis is a linear superposition of the field generated for each discretized region, each of which can be written in terms of Lommel functions [16]. Also shown is the contribution from secondary reflections within the lens. This fraction is modeled by including a second lens at the pupil plane with a focal length of 60.8 mm (the combination of two lenses of 654 and 67 mm) and transmission factor of 0.047^2 to account for Fresnel losses. The inset graph shows the predicted signal intensity at 0.5° from the optical axis as the entrance window radius is varied from the optimal value of 1.25 mm, where the aperture radius is equal to the radius of the primary lobe.

achieve the maximum roll-off, even after mapping the beam profile at the pupil. Figure 3-7 compares the measured background signature with the expected profile based on the aerial image simulations for the case where the entrance window is 2 mm larger than the radius of the first lobe. The measured background signal is in good agreement with the theory.

In performing measurements over 7 orders of magnitude, attenuators are cycled into the beam line rather than modulating the bias voltage of the PMT. Attenuators are fabricated by depositing a thin film of platinum on CaF_2 . The attenuators have a transmission range between 15 and 40% and are calibrated individually in situ using the PMT. The standard deviation over seven separate measurements is approximately 5%. Since there are ten separate attenuators, the cumulative uncertainty due to these variations is the principal source of error in determining the absolute value of the scattered light.

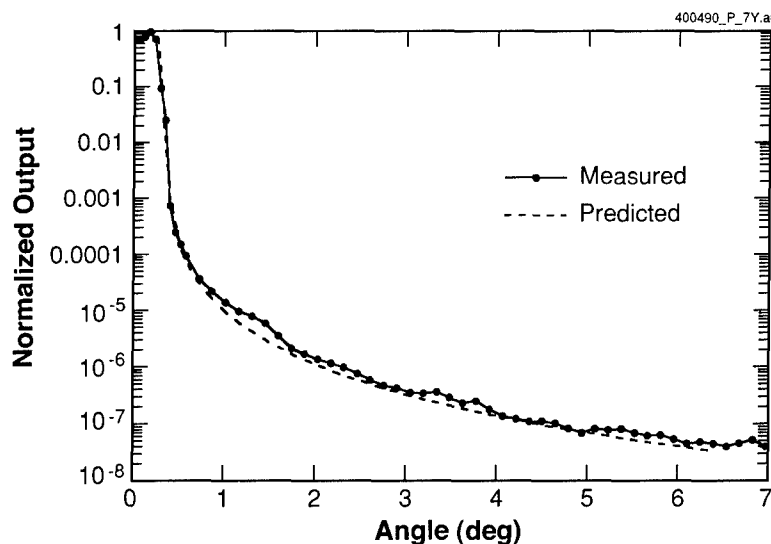


Figure 3-7. Comparison of predicted and measured background signal for the 2 \times imaging system using a 100- μ m pinhole in the object plane. The predicted curve is calculated by convolving the aerial image that is formed when the entrance window is 2 mm larger than the radius of the first lobe and the detector has a 2-mm-diam circular aperture.

In addition to performing scattering measurements over large angles with a PMT on the goniometer, we also mounted a PMT on a three-axis XYZ stage. This detector can be scanned in both x and y directions, and therefore two-dimensional mappings can also be made, to look for anisotropies in the scattered signature. To test this capability, the diffraction pattern from a 12.5- μ m period grating fabricated in CaF₂ was measured. The grating was patterned with contact lithography followed by reactive ion etching. Figure 3-8 shows a cross-sectional view of a portion of the grating measured with AFM. The etched step height is ~ 6.25 nm. However, as evident in the AFM profile in Figure 3-8, significant levels of material were redeposited along the sidewalls during the etching process. Therefore, 10-nm-high “hills” appear in the AFM traces, with a full period of 6.25 μ m, half that of the grating. A two-dimensional contour plot of the diffraction pattern measured with the small angle component of the scattering system is shown in Figure 3-9. A slice that intersects the diffracted lobes is shown in Figure 3-10. For a perfect square wave, only odd diffractive orders are expected. Since the redeposited material repeats at twice the frequency of the grating, it accounts for the presence of the second-order peaks shown in Figure 3-10. These results also confirm that the angular sensitivity of the ARS system can be extended to 0.5° or less, but at these angles it is capable of detecting scattered intensities that are $\sim 10^{-5}$, or higher, of the specular beam, rather than the $\sim 10^{-7}$ at larger angles.

We have begun to use this system to evaluate optical materials and coatings. In general, the correlation between forward scattering and the degree of surface roughness has been found to correlate better on antireflective coatings than on CaF₂ surfaces. Estimates on the degree of flare indicate that it may

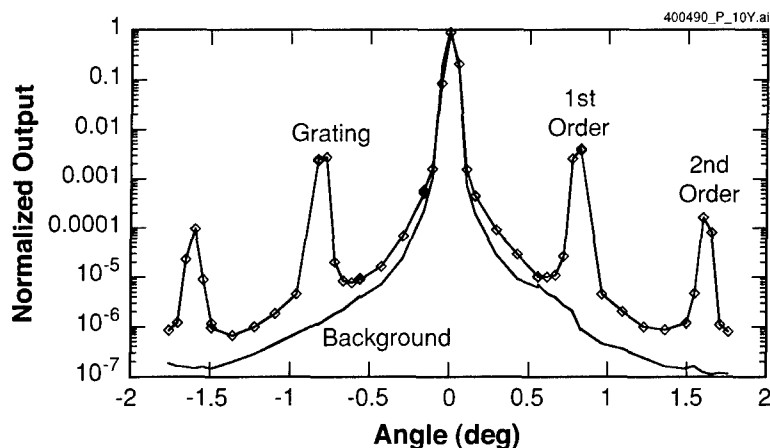


Figure 3-10. Measured intensity of a single line scan that transverses the diffracted orders formed by the grating. The scan was extended to encompass the second-order lobes. Also shown are the expected locations of each peak and the expected intensity of the first lobe. For a perfect grating, this intensity level is approximately equal to the square of the product of the wave number times the amplitude of the grating. The measured intensity is lower by a factor of 5, presumably because of the loss of energy into the second order.

impact lithographic process latitude. In the future, we plan on improving the measurement capabilities at small angles to better establish the extent of light scattered within a few to several hundred microns from bright fields in a high-performance stepper lens.

T. M. Bloomstein D. E. Hardy
L. Gomez M. Rothschild

REFERENCES

1. V. I. Klykov and N. N. Sheftal, *J. Cryst. Growth* **52**, 687 (1981).
2. D. C. Flanders, Ph.D thesis, Massachusetts Institute of Technology, 1978; MIT Lincoln Laboratory Technical Report No. 533.
3. H. I. Smith, M. W. Geis, C. V. Thompson, and H. A. Atwater, *J. Cryst. Growth* **63**, 527 (1983).
4. M. W. Geis, D. A. Antoniadis, D. J. Silverman, R. W. Mountain, and H. I. Smith, *Appl. Phys. Lett.* **37**, 454 (1980).
5. L. S. Darken and D. H. Lowndes, *Appl. Phys. Lett.* **40**, 954 (1982).
6. S. Miyazawa and M. Mukaida, *Appl. Phys. Lett.* **64**, 2160 (1994).

7. Ch. Bosshard, *Organic Nonlinear Optical Materials* (Gordon and Breach, Basel, 1995), Chap. 4.
8. S. Sohma, H. Takahashi, T. Taniuchi, and H. Ito, *Chem. Phys.* **245**, 359 (1999).
9. Y. Mori, Y. Takahashi, T. Iwai, M. Yoshimura, Y. K. Yap, and T. Sasaki, *Jpn. J. Appl. Phys.* **39**, L1006 (2000).
10. N. Shopova and T. Milkova, *Thermochim. Acta* **356**, 101 (2000).
11. S. R. Marder, J. W. Perry, and W. P. Schaefer, *Science* **245**, 626 (1989).
12. K. Lai, C. Wu, and C. Proglar, *Proc. SPIE* **4346**, 1424 (2001).
13. J. P. Kirk, *Proc. SPIE* **2197**, 566 (1994).
14. C. Proglar and A. Wong, *Proc. SPIE* **4000**, 40 (2000).
15. H. Bartelt, S. Brückner, C. Chojetzki, D. Müller, E. Ose, H. Stafast, and W. Triebel, *LaserOpto* (AT-Fachverlag, Germany) **33**, 58 (2001).
16. M. Born and E. Wolf, *Principles of Optics* (Pergamon, New York, 1965), pp. 435–442.

4. BIOSENSOR AND MOLECULAR TECHNOLOGIES

4.1 BIOSILICON INTEGRATION

Living cells have evolved to be able to conduct rapid, complex, and highly specific bioelectrochemical interactions with their environment via protein receptors and ion channels on the cell membrane surface. Potentially, much benefit can be derived from combining the sensitivity and specificity of these biological interactions with such attributes of modern electronic devices as rapid, massively parallel, high-speed signal processing and conversion. The key to such an endeavor is the approach taken towards the integration of the two areas. Our approach, described here, is to achieve this merging with the construction of an artificial biomolecular platform, in which useful “components” from the cell are reproduced in a more robust framework and coupled to silicon circuits. Such a system could provide the enabling technology base for new classes of biological and chemical detectors and other biodevices, and on a more basic level it can also serve as a platform for study of the fundamental structure and function of cellular and membrane-bound proteins.

Many of the biochemical receptors used by the cell to interact with its environment reside in the external cell membrane. The cell membrane is a bilayer lipid membrane (BLM), composed of a double layer of amphiphilic phospholipid molecules, structurally arranged as shown in Figure 4-1. As such, the formation of a stable BLM is vital to the implementation of an artificial, engineered biosystem. In a living cell, membrane stability and integrity are maintained continuously by cellular processes. We are developing a micromachined device, referred to as the membrane maker, that will be capable of forming BLMs, monitoring them, and regenerating them when necessary, all in an autonomous fashion. Once formed, the BLM may be functionalized with membrane-bound proteins that have been purified and inserted from solution. By this approach, we will be able to produce and utilize cellular receptors without having to maintain unused portions of the cellular infrastructure. Additionally, we can study and

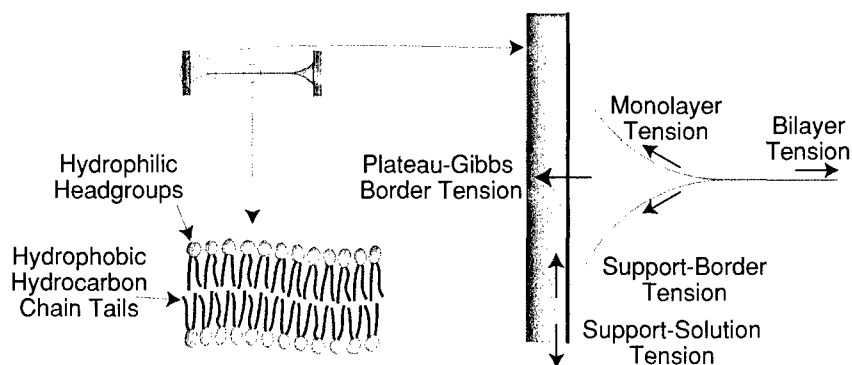


Figure 4-1. Bilayer lipid membrane (BLM) structure and support.

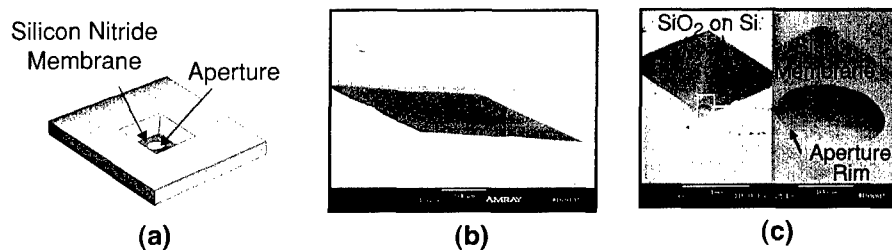


Figure 4-2. Micromachined silicon nitride apertures: (a) diagram of back side of chip, (b) scanning electron micrograph (SEM) of front side of chip showing aperture, and (c) SEM of back side of chip showing closeup of aperture.

manipulate these molecules, as well as construct arrays of receptors for large-scale sensing functions or studies of protein interactions. Among the applications that will be enabled by such artificially generated cell membranes are cell-like sensors, ion-channel sensors, DNA sensors and sequencers, and protein synthesis and design.

The central element in the membrane maker is a micromachined aperture, which serves as the substrate for the BLM. This aperture is fabricated using conventional silicon micromachining techniques, and consists of a silicon chip coated with a thin (80 nm) silicon nitride membrane with a circular opening, as illustrated in Figure 4-2. After the membrane is formed, the exposed silicon on the back side of the chip is passivated with a layer of low-temperature-deposited silicon dioxide ~100 nm in thickness. A coating of hexamethyl disilazane is added to the front surface of the chip to render the silicon nitride surface hydrophobic prior to use.

We investigated two approaches to BLM formation. The first is the lipid-droplet approach, analogous to traditional “painted bilayer” methods [1] used by biologists to form BLMs, in which a small volume of lipid in solvent is placed onto an aperture in a hydrophobic surface submerged in an aqueous solution. The BLM is formed on an aperture consisting of two micromachined silicon nitride openings separated by a spacer. The spacer also defines a channel to contain excess phospholipid material. The phospholipid molecules, dissolved in a solvent, are dispensed from above the aperture in the form of a droplet of material. The droplet anchors onto the aperture edges, which have been treated with a surface coating to render them hydrophobic. Once anchored, they begin the self-assembly process, aided by capillary action pulling excess phospholipid into the side channels. During the formation process, the membrane is monitored via capacitance and ionic current measurements through the use of two thin film electrodes located above and below the aperture.

Figure 4-3 shows the setup that was constructed to perform optical and electrical measurements using the lipid-droplet approach. It is a simplified version of the schematic membrane maker, in which the nitride apertures are held in a Teflon jig containing access ports for lipid dispensing (manually via a

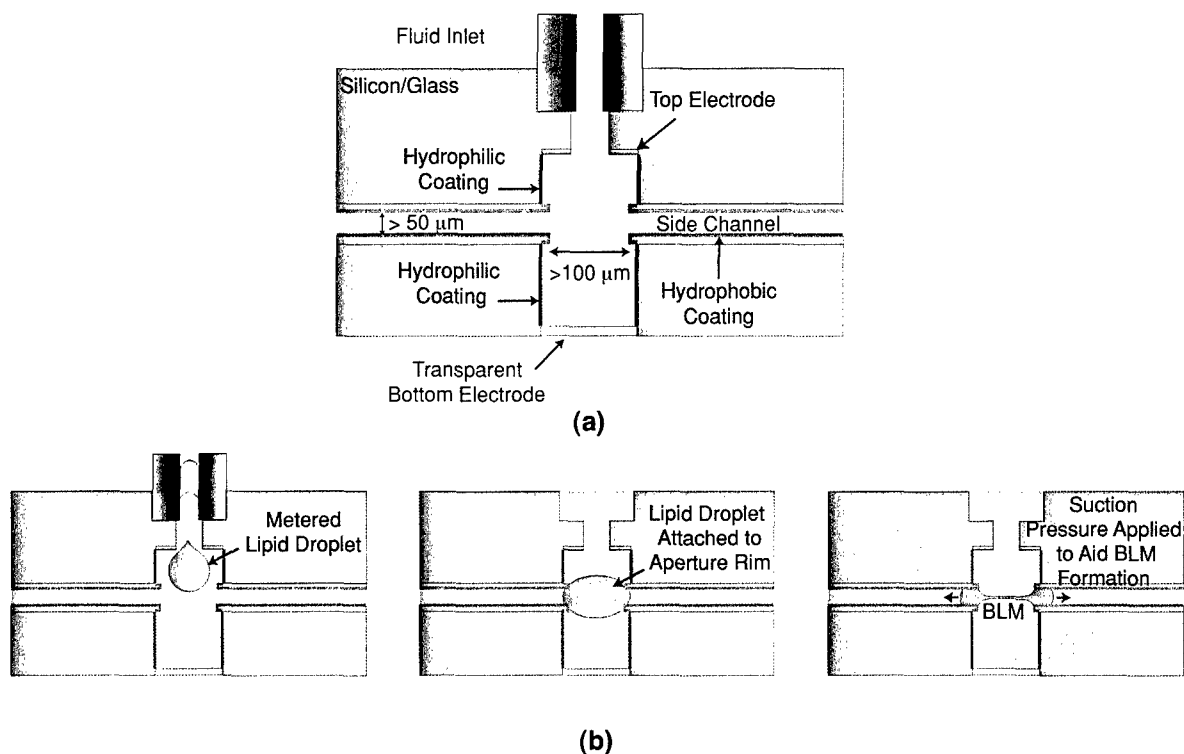


Figure 4-3. Conceptual schematics of (a) membrane maker and (b) BLM formation procedure.

syringe). The membrane is pressurized from below using a threaded syringe. Electrical contact to both sides of the membrane is achieved via Ag/AgCl wires placed in contact with the aqueous solution surrounding the aperture.

For optical observation, once the lipid was dispensed into the aperture using the setup in Figure 4-4, the syringe was removed and the aperture monitored in an optical microscope. Figure 4-5 shows the progressive increase in thinned membrane area at the center of an aperture of diameter 1 mm. In this example, the lifetime of the membrane was limited (< 6 min), owing to the use of chloroform as the solvent for the lipid.

Thinning was also observed via capacitance measurements of the membrane as it approached the bilayer state. Capacitance was obtained by applying a triangular voltage waveform across the aperture. The amplitude of the output current square waveform is proportional to the capacitances of the membrane plus the surrounding solution and sidewalls. Figure 4-6 shows the input voltage waveform and two representative output capacitance-time plots. In Figure 4-6(a), after the initial dispensing of the lipid into the aperture the capacitance value is low, and as thinning progresses the value increases. Suction is applied from the back side of the aperture to remove excess lipid and produce a fully thinned BLM, as indicated by

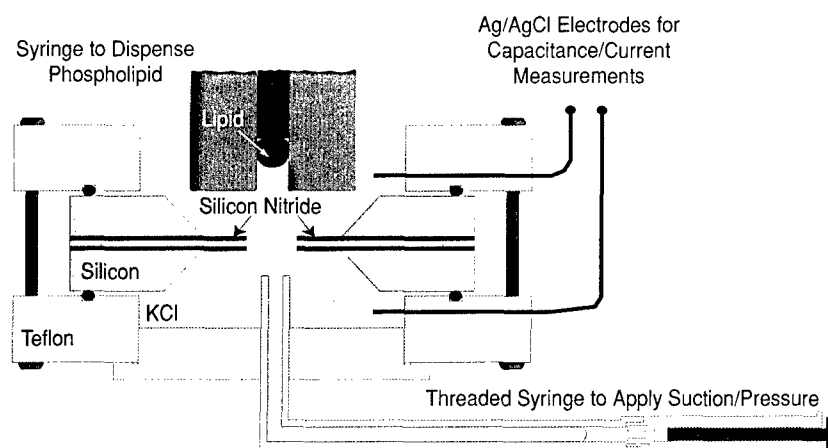


Figure 4-4. Test jig for conducting membrane capacitance measurements.

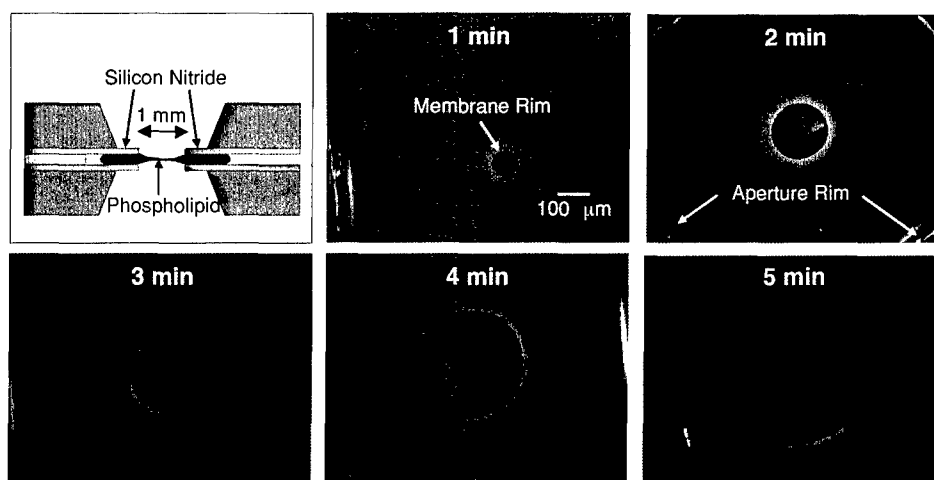


Figure 4-5. Membrane formation as observed in optical microscope. Phospholipid is phosphatidyl ethanolamine (10 mg/mL) in chloroform; aqueous solution is 0.1M NaCl at room temperature.

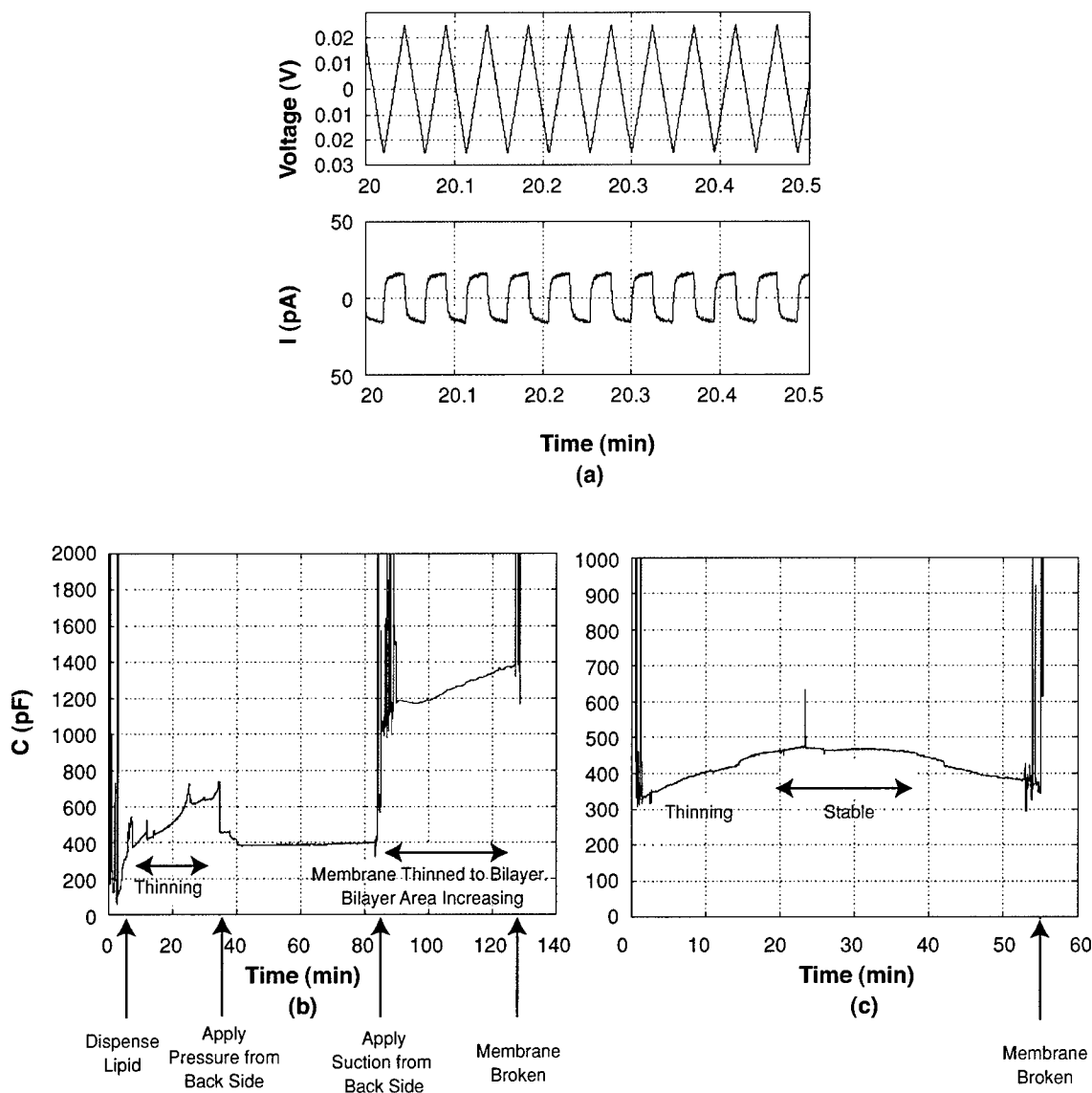


Figure 4-6. Examples of measured capacitance of membranes: (a) Triangular voltage input signal and square current output signal across membrane. Input is applied and output measured with a Keithley 6430 source meter. (b) Measured current and capacitance across membrane ($I = C dV/dt$) formed in 140- μm -diam aperture. Lipid is $\sim 3\text{-}\mu\text{L}$ phosphatidyl ethanolamine (5 mg/mL) in *n*-decane. Aqueous solution is 0.1M KCl at 30°C. Back-side fluid pressure is varied with a threaded syringe. The application of positive pressure increases membrane thickness and decreases capacitance; suction decreases membrane thickness by pulling excess lipid away from the aperture and increases capacitance. (c) Measured current and capacitance across membrane formed in 80- μm -diam aperture. Lipid is $\sim 3\text{-}\mu\text{L}$ phosphatidyl ethanolamine (10 mg/mL) in *n*-decane. Aqueous solution is 0.1M KCl at 30°C.

TABLE 4-1
Parameters for Optimal Membrane Formation Time and Stability

Parameter Space:	
Aperture Diameters	80, 140, 180, 300, 1000 μm
Lipids	Egg phosphatidyl choline (EPC), phosphatidyl ethanolamine (PE)
Solvents	Chloroform, <i>n</i> -decane, tetradecane, hexane
Concentrations	1–25 mg/mL
Aqueous Solution	0.1M KCl
Aqueous Solution Temperatures	20°C, 35°C
Optimal Parameter Set:	
Aperture diameter	<180 μm
Lipids	EPC 2–5 mg/mL in <i>n</i> -decane, PE 5–10 mg/mL in <i>n</i> -decane,
Aqueous solution	0.1M KCl
Aqueous solution temperature	35°C

a rapid increase in capacitance. After this point the BLM area increases, as indicated by a more gradual increase in capacitance. Figure 4-6(b) shows another representative measurement, in which no pressure was required to reach a thinned state. By using the set of variables shown in Table 4-1, capacitance measurements were conducted to determine parameters for optimal membrane formation time and stability. Membrane formation time was minimized for lower concentrations of lipid using *n*-decane as the solvent and heating the aqueous solution.

Our second approach, the vesicle-formation approach, was demonstrated with another laminated test structure. A vesicle (liposome) is a bilayer lipid bubble, and is essentially a cell without its contents, as shown in Figure 4-7. Vesicles are commonly used in molecular biology for delivery of nucleic acids, proteins, peptides, and other biological molecules into cells, and are particularly appealing for drug delivery applications. With the insertion of surface proteins from bioagents into the membrane, they can also serve as bioagent simulants. As an alternative method for producing BLMs, we investigated forming and anchoring vesicles onto the silicon nitride aperture. This method can result in a shorter BLM formation time and also ensures that the membrane is indeed a bilayer and not a multilayer stack, as can be the case for the lipid-droplet approach in which excess lipid is always present initially.

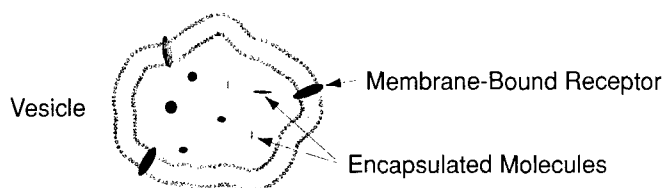


Figure 4-7. Structure of vesicle (liposome).

We formed vesicles from rehydrated films of phospholipid in the presence of an electric field. This technique has been successfully utilized in the formation of large ($10\text{--}100\ \mu\text{m}$) unilamellar vesicles [2],[3]. A device using the dry-film approach may be more suitable for eventual long-term storage and field use, since it can enable the use of protein channels that are unstable in solution phase but can be stably stored in lyophilized (dry) format. The micromachined structure shown in Figure 4-8 was used to demonstrate vesicle formation. It consists of the previously described silicon nitride aperture packaged between glass plates with thin film electrodes (either platinum or indium-tin oxide). The lipid is present in the form of a dried film on the electrode surface. Upon hydration in a salt solution and application of an electric field ($<5\ \text{V/mm}$), vesicles are generated and separated from the electrode surface. If the liposome diameter is equal to the height of the channel above the silicon nitride aperture, it can fuse with the aperture edge, similar to conventional patch-clamp pipette methods. The formation of a good seal can be monitored via current measurements across the aperture.

With the vesicle-formation approach, vesicles were formed from naturally occurring lipids and attached to micromachined apertures. Several examples are shown in Figure 4-9. Attachment was indicated by the cessation of fluid and excess vesicle flow across the aperture. We demonstrated vesicle formation using two electrode types—ITO and platinum—and two lipid types—phosphatidyl ethanolamine (PE) and dioleoyl phosphatidyl glycerol with sodium salt (DOPG-Na), a charged lipid.

Thus, we have developed two methods for forming BLMs, the lipid-droplet and vesicle-formation approaches. We have also resolved a number of device and packaging issues; have developed a packaging scheme with polydimethyl siloxane channels, thin film metal electrodes, and silicon nitride apertures; and have exercised these packaged devices by particle counting of polystyrene beads. The basic structures and test setups for investigating ion-channel insertion and behavior have been established.

L. Parameswaran

REFERENCES

1. M. Montal and P. Mueller, *Proc. Natl. Acad. Sci. USA* **69**, 3561 (1972).
2. M. Angelova and D. Dimitrov, *Faraday Discuss. Chem. Soc.* **81**, 303 (1986).
3. L. Mathivet, S. Cribier, and P. Devaux, *Biophys. J.* **70**, 1112 (1996).

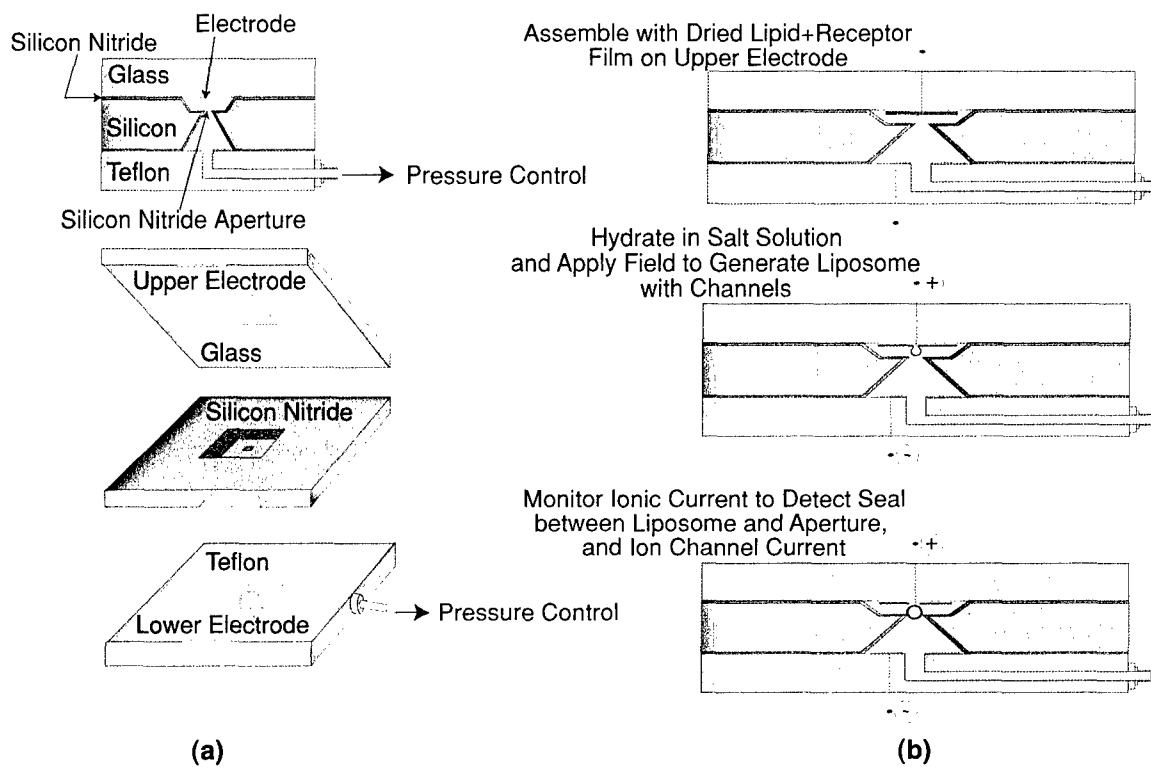


Figure 4-8. (a) Micromachined structure and (b) liposome formation and ion-channel-current measurement.

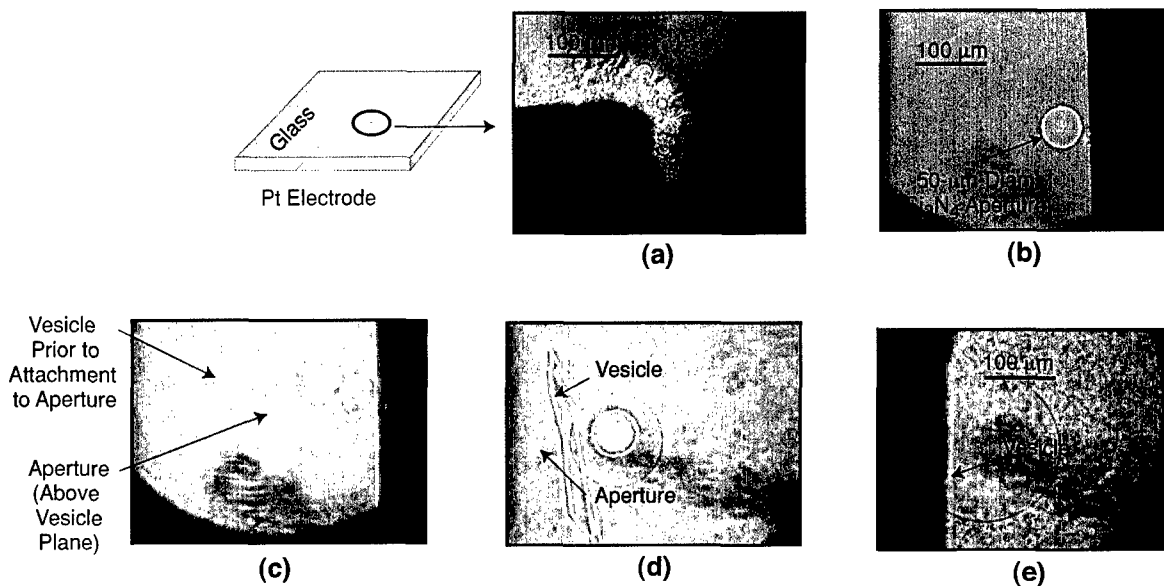


Figure 4-9. Phase contrast micrographs of vesicles generated from rehydrated dried lipid films: (a) Lipid is phosphatidyl ethanolamine at 10 mg/mL in chloroform, 0.5 μL deposited on Pt electrode, rehydrated in distilled water with 2 V_{dc} across 2-mm gap. Image is taken at the corner of Pt electrode. (b) Silicon nitride aperture seen from above through upper ITO electrode. (c)–(e) Lipid is DOPG-Na at 10 mg/mL, 0.5 μL deposited on ITO lower electrode, rehydrated in distilled water. Shown are (c) vesicle before attachment to aperture, 7 V_{dc} across 3-mm gap, (d) vesicle attached to aperture, 5 V_{dc} across 3-mm gap, and (e) large unattached vesicle, 5 V_{dc} across 3-mm gap.

5. ADVANCED IMAGING TECHNOLOGY

5.1 CMOS TIMING CHIP FOR THREE-DIMENSIONAL IMAGING WITH GEIGER-MODE AVALANCHE PHOTODIODES

Conventional laser radar (ladar) imaging systems are based on mechanically scanning the field of view of a single-channel optical radar over the scene of interest. Scanning severely limits the data acquisition rates of such systems. An alternative architecture is the flash ladar, which images the scene onto a focal plane array, each pixel of which measures the flight time of the transmitted pulse. A flash system can acquire a ladar image with a single laser pulse and without moving parts. Because it divides the transmitted energy over many pixels, however, it places stringent demands on photodetector sensitivity. Lincoln Laboratory has demonstrated flash ladar systems based on arrays of Geiger-mode avalanche photodiodes (APDs) integrated with all-digital per-pixel CMOS timing circuits [1],[2]. The Geiger-mode APD is operated to produce a digital voltage signal upon detection of as little as a single photon, and the pixel circuit records the time of this event by stopping a high-speed counter. This final counter value encodes the range to the corresponding point in the scene. The resulting combination of single-photon sensitivity and subnanosecond timing enables compact high-performance ladar systems.

The pixel circuit architecture must not only support the time measurement performance but must also take up minimum chip real estate and facilitate data readout that supports desired frame rates. It should also enable the focal plane to be scaled up to larger formats. We discuss the design and performance of CMOS timing chips that have been used to build fully functional 32×32 ladar focal planes with 0.5-ns timing resolution.

The architecture of the pixel circuit, illustrated in Figure 5-1, uses a high-speed digital counter to measure time, and refines that measurement by generating two vernier bits that encode the detection-time phase of the clock that drives the counter. A 500-MHz master clock is generated on chip and broadcast to all pixels. In each pixel, the clock drives the counter through a tri-state inverter. The detection pulse from the APD puts this inverter into its high-impedance state, which stops the counter and stores the detection-time clock state on the capacitance at the inverter output. Thus, the detection time is digitized to a resolution of half the clock period. A secondary clock is generated by delaying the master clock by 90° in phase and is broadcast to all the pixels. The detection-time state of the secondary clock is also captured by a tri-state inverter, which allows for quantization of the detection time to a resolution of one fourth the clock period. This corresponds to a ladar range resolution of 3 in. (7.6 cm).

This architecture must be implemented as compactly as possible. Therefore, the counter is a pseudo-random counter rather than a conventional binary counter. The pseudo-random counter is a shift register with a feedback path that has an exclusive-OR gate; if the shift register is n bits long, it cycles through a sequence of $2^n - 1$ distinct states. The state of the counter thus encodes the number of clock cycles that have elapsed from the start of counting to the photon detection time. This approach yields a compact

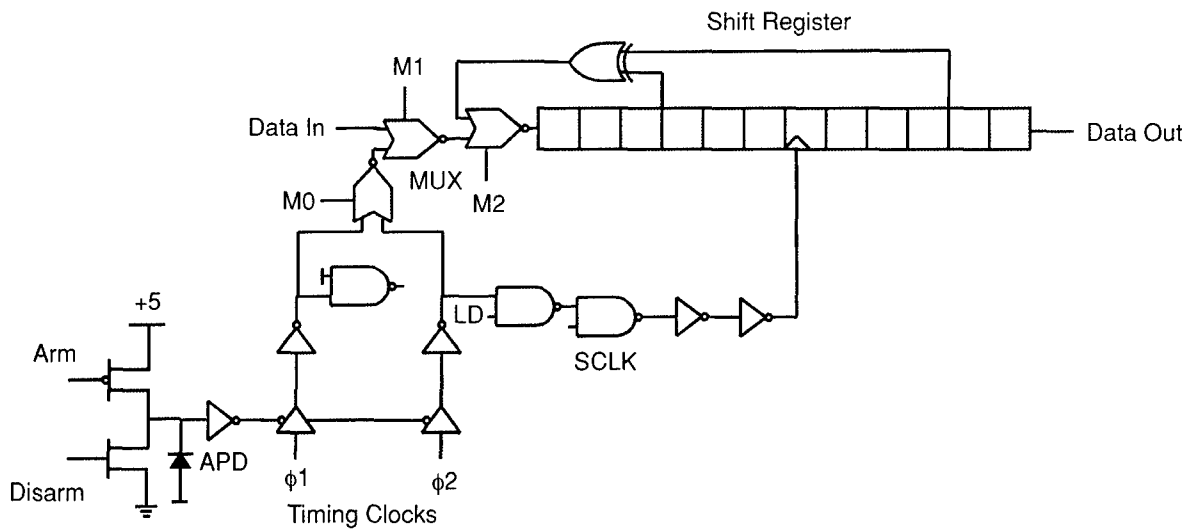


Figure 5-1. Logic diagram of pixel circuit of lidar focal plane.

pixel circuit because the same flip-flops are used for counting, storage, and readout. Multiplexers are included in the circuit to switch from time measurement mode to readout mode. In readout, the stored clock states are first shifted into the shift register, which has two extra flip-flops to accommodate this. Then the shift registers along each row of pixels are daisy chained (“data out” of each pixel goes to “data in” of the next one) and read out serially.

The vernier bit scheme facilitates achievement of subnanosecond precision without requiring 2-GHz clocking. Therefore, one can use an established commercial foundry process with 0.5- or 0.35- μm gate geometries. A 16-pixel array using a 17-bit version of the counter circuit was demonstrated using a MOSIS 0.5- μm CMOS process, and 32×32 arrays of 10- and 15-bit counter circuits have been demonstrated using a MOSIS 0.35- μm process. The most recent version of the 32×32 chip operates stably at clock speeds up to 650 MHz, and achieves the 0.5-ns timing resolution goal.

The APD biasing and sensing scheme also supports a simple, compact pixel circuit. The p side of the APD is biased at a negative voltage whose magnitude is just below the avalanche breakdown. Assertion of the ARM signal causes the n sides of all the APDs to be pulled up to +5 V, thereby biasing them several volts above breakdown. When a photon is detected by an APD, the resulting avalanche discharges it to the breakdown voltage, an event that is interpreted by a sensing inverter as a logic high-to-low transition. This voltage sensing scheme introduces more delay and timing jitter than circuits based on sensing the rise of the APD current [3], but is much simpler, is CMOS compatible, and requires no analog circuitry.

Assertion of the DISARM signal causes the n side of each APD to be pulled down to 0 V, thereby turning the APD “off.” Even when the CMOS circuit has not been integrated with APDs, however, the DISARM signal electronically simulates a detection event, which is useful in testing. The DISARM signal

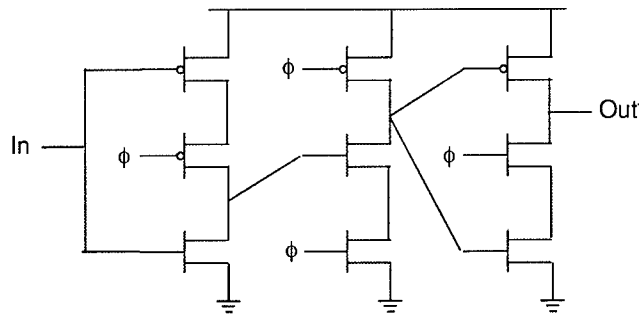


Figure 5-2. D flip-flop circuit that forms the building block of the pixel counter.

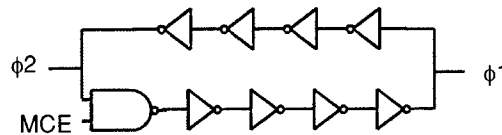


Figure 5-3. Logic diagram of ring oscillator that produces the master clock and the 90°-delayed clock.

propagates across the chip with a delay of about 1.5 clock cycles so that the resulting image has a gradation of timing values. The device range data can be processed off-chip to remove the clock delay bias.

The pixel logic operates from a 3.3-V supply. The APD is operated with a 5-V swing because its photon detection probability increases monotonically with bias; a bias of 4–5 V above breakdown is needed to achieve high detection probability. The CMOS foundry process supports both 5- and 3.3-V transistors for mixed-mode circuits. The arm/disarm circuit and the APD sensing inverter are fabricated with the higher-voltage transistors. The sensing inverter, which operates from the 3.3-V supply, performs the necessary voltage level shifting function.

The circuit for the D flip-flop in the shift register is shown in Figure 5-2. This is known as a true single-phase clocking (TSPC) architecture [4]. It is a dynamic master-slave flip-flop that requires only a single clock phase. The leftmost branch of the circuit is the master stage, and the other two branches constitute the slave. When the clock is low, the master evaluates (and inverts) the input signal, while the output of the slave is in the high-impedance state. When the clock rises, the result of the master's evaluation propagates to the slave output. The TSPC flip-flop is amenable to a compact layout and is free of race conditions as long as the clock edges are sharp.

Figure 5-3 shows the ring oscillator circuit used to generate the 500-MHz timing clock. Once the APDs have been armed and the timing circuits are ready to count, the clock is turned on by asserting the MCE (master clock enable) signal. By using a NAND gate in the ring oscillator to start the clock rather than gating a continuous clock with an asynchronous control signal, start-up glitches are avoided. The

power supplies for the ring oscillator are separate from those for the rest of the chip, allowing for tuning of the ring oscillator frequency.

In previous versions of the circuit, the 90°-delayed clock was generated by feeding the ring oscillator output into a voltage-controlled delay stage. It was found, however, that the rising and falling edges are delayed by different amounts, resulting in duty cycle skewing and uneven vernier time bins. The scheme employed in the current architecture is to simply tap the two clocks off of opposite ends of the ring oscillator. This yields a phase difference that is very close to 90° without subjecting either clock to delay elements that degrade the rise or fall times or skew the duty cycle. The upper and lower branches of the ring oscillator are powered separately, allowing for fine tuning of the phase difference. Each clock is distributed to both ends of each row of pixels by clock distribution trees that have a fanout of two at each stage.

A separate clock (SCLK) generated off chip is used for readout. There are 16 outputs, one for each adjacent pair of rows. During each cycle of the SCLK, a 2-to-1 multiplexer on each output is used to select the next bit from the odd-numbered row and then from the even-numbered row. De-interleaving and decoding are accomplished off chip. The chip has been operated in ladar systems at frame rates of 20 kframes/s (corresponding to modest SCLK frequencies <8 MHz). The architecture is capable of supporting much higher frame rates (hundreds of kframes/s) for the 32 × 32 array, and the frame readout time scales linearly with the number of pixels per row.

Figure 5-4 shows a photograph of the chip and Figure 5-5 a magnified view of one pixel circuit. The pixel pitch is 100 μm, but the circuitry occupies only about half the pixel area. The white square in each pixel is the pad where the connection to the corresponding APD is made. Much of the pixel area is used for power supply decoupling capacitors (the horizontal stripes in the top half of the pixel). There are also decoupling capacitors throughout the clock distribution tree and near the power and ground bonding pads at the chip periphery. The clock speed on previous versions of the chip was limited by ground bounce because of the parasitics associated with the power supply rails. The current chip has wider rails with more decoupling capacitance and operates stably at clock speeds up to 650 MHz.

Figure 5-6 shows a grey-scale ladar image obtained by operating a chip at 500 MHz without APDs and using the propagation of the DISARM signal to produce a gradation of timing values. Rather than showing the absolute timing values, the grey scale encodes one of the four possible states of the two vernier bits. The relatively uniform widths of the contour bands in this image show that the vernier bits function properly, dividing the clock period into four roughly equal intervals.

Thus, we have demonstrated an all-digital timing chip for ladar focal planes using Geiger-mode APDs. The chip is scalable to larger formats, operates at high frame rates, and supports photon flight time measurements with 0.5-ns resolution. The focal planes fabricated using this chip have been used to build functional flash ladar systems that have collected imagery in a number of field tests. Future work will focus on making the pixel even more compact while refining its timing resolution.

B. F. Aull

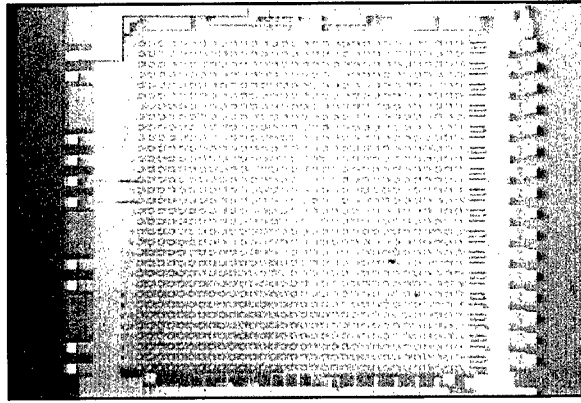


Figure 5-4. Photograph of 32 × 32 CMOS timing chip.

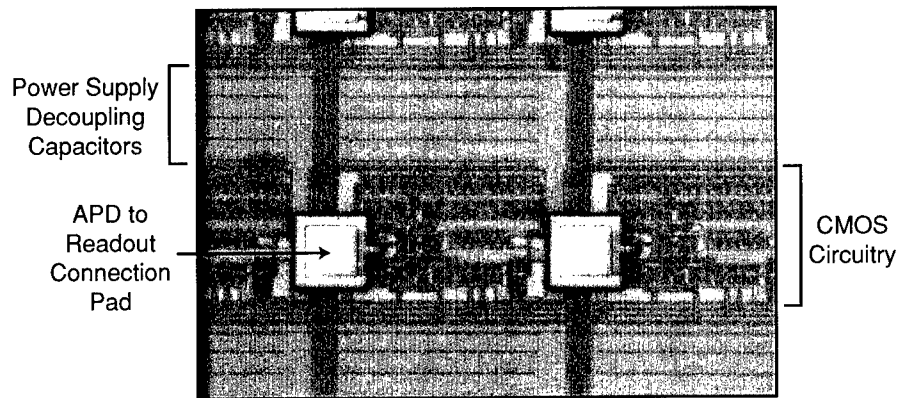


Figure 5-5. Photograph of single pixel of the CMOS timing chip.

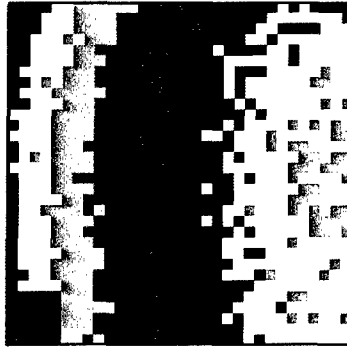


Figure 5-6. Grey-scale image showing the state of the vernier timing bits in response to electronic triggering of the timing chip using the DISARM signal.

REFERENCES

1. B. F. Aull, A. H. Loomis, D. J. Young, R. M. Heinrichs, B. J. Felton, P. J. Daniels, and D. J. Landers, *Linc. Lab. J.* **13**, 335 (2002).
2. M. A. Albota, B. F. Aull, D. G. Fouche, R. M. Heinrichs, D. G. Kocher, R. M. Marino, J. G. Mooney, N. R. Newbury, M. E. O'Brien, B. E. Player, B. C. Willard, and J. J. Zayhowski, *Linc. Lab. J.* **13**, 351 (2002).
3. S. Cova, M. Ghioni, A. Lacaita, C. Samori, and F. Zappa, *Appl. Opt.* **35**, 1956 (1996).
4. J. M. Rabaey, *Digital Integrated Circuits: A Design Perspective* (Prentice Hall, Upper Saddle River, N.J., 1996).

6. ANALOG DEVICE TECHNOLOGY

6.1 QUANTUM FLUX PARAMETRON AS A READOUT ELEMENT FOR A PERSISTENT-CURRENT QUBIT

The persistent-current qubit is one realization of a quantum-mechanical two-state system [1],[2]. It is a superconducting loop comprising three Josephson junctions. The junction sizes are designed such that the clockwise and counterclockwise persistent currents around the loop are the asymptotic states of a coupled, two-state system (double-well potential). Such a system exhibits macroscopic quantum coherence: for example, quantum superposition [3] and spin echo experiments [4] have been demonstrated using these macroscopic qubits. Because these devices may be fabricated in a planar geometry with the corresponding possibility of large-scale integration, the persistent-current qubit is a leading candidate to be the fundamental quantum logic element in a quantum computer.

A key element of any qubit technology is the readout device. In general, a readout device comprises a quantum probe and a classical meter. The quantum probe becomes entangled with the qubit and, later, a classical meter reads out the state of the probe. This process projects the entangled probe-qubit system onto a specific correlated state. The acquisition of information in this manner is called a projective measurement. Repeated projective measurements on identically prepared quantum systems provide a statistical description of the state of the quantum system. A dc superconducting quantum interference device (SQUID) loop surrounding a persistent-current qubit is one common example of a readout device. The dc SQUID is a sensitive magnetometer that senses a change in flux due to a change in the qubit persistent-current state. An alternative readout device that may offer advantages over the dc SQUID in terms of readout sensitivity, readout speed, and qubit isolation is the quantum flux parametron (QFP).

The QFP, shown in Figure 6-1(a), is a sensitive current comparator [5]. The main components of a QFP are (1) the QFP arms, each with a Josephson junction with critical current $i_{c1} = i_{c2}$; (2) the QFP spine, which carries the current i_s that the QFP comparator will discriminate; (3) the QFP exciter, which initiates a QFP comparator discrimination of the spine current i_s ; and (4) the QFP readout SQUID, which reads out the state of the QFP comparator. An offset current source connected to the spine provides a means to tune the QFP comparator. A persistent-current qubit and the qubit bias line are also shown in Figure 6-1.

Consider a fixed spine current i_s with a particular direction (current polarity) up or down the QFP spine. An ideal QFP comparator discriminates the direction of i_s ; its operation may be conceptually understood in the following manner. The spine current i_s splits equally along the two arms of the QFP. A measurement is initiated by ramping up a large current in the QFP exciter line. This induces currents in the QFP arms, which will superpose with the split currents from the spine. The currents are additive in one of the arms and subtractive in the other arm, depending on the direction of i_s . As the induced exciter current increases, the junction in the arm with the additive currents will exceed its critical current before the junction in the arm with the subtractive current. Exceeding the critical current causes the addition of a

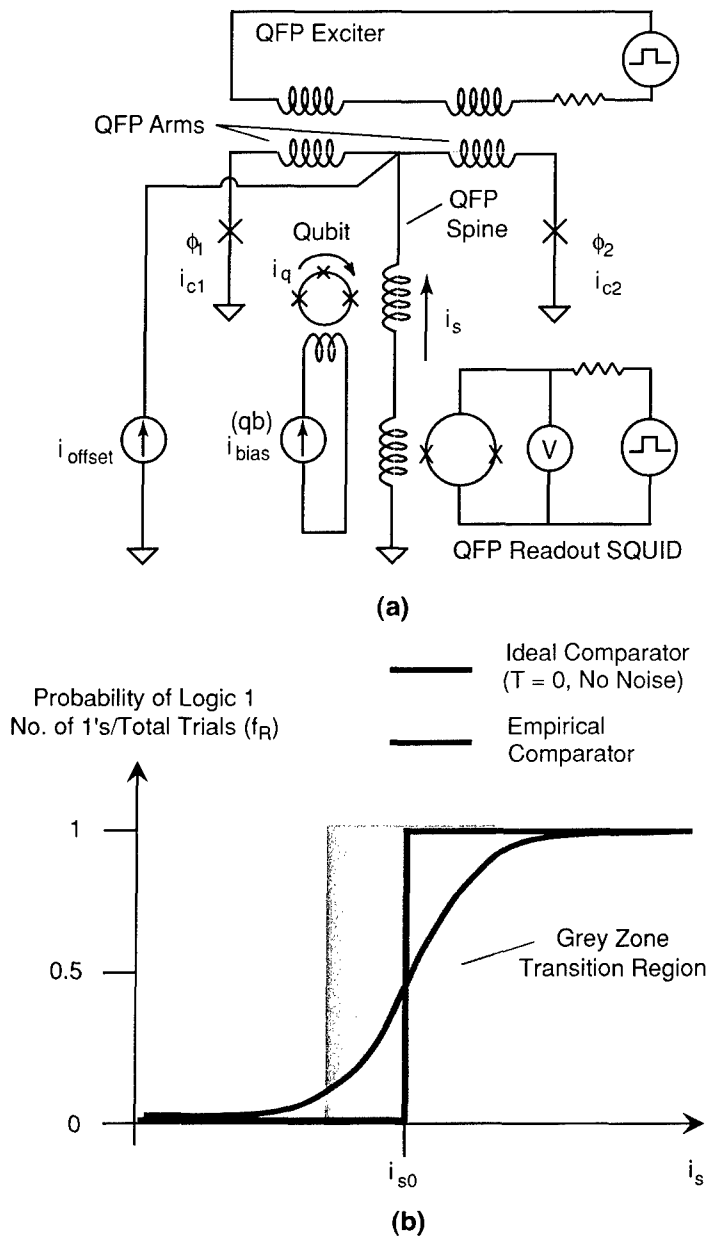


Figure 6-1. (a) Schematic of quantum flux parametron (QFP) comparator. The comparator includes the QFP arms, QFP spine and offset current, QFP exciter line, and QFP readout superconducting quantum interference device (SQUID). The comparator is used to read out the state of a persistent current qubit. The qubit is biased, and it induces a current into the spine, which is subsequently discriminated by the QFP. (b) Grey zone for a QFP comparator. The ideal grey zone is a step function. The presence of noise results in a distribution of spine currents, which leads to a grey zone when the comparator output is averaged over many trials. The slope of the grey zone at the 50% point, i_{s0} , is a figure of merit for the comparator.

fluxon to the loop formed by the spine and the arm with the junction that exceeded its critical current. The addition of the fluxon results in a large current being sent along the spine; the direction of this new and amplified spine current $i_s^{(\text{amp})}$ is correlated with the initial spine current, $i_s^{(\text{amp})} = Ai_s$. In this sense, the QFP may be viewed as an amplifier. Finally, the discrimination of the QFP state, that is, the direction of the amplified current $i_s^{(\text{amp})}$, is realized using a dc SQUID readout. The SQUID is biased such that one direction of the amplified spine current will result in a large voltage drop across the SQUID (arbitrarily denoted as logic 1), while the other direction will not (logic 0). A voltage meter records the presence or absence of the SQUID readout voltage. Because the amplified and initial spine currents are correlated, $i_s^{(\text{amp})} = Ai_s$, the measurement of logic 1 or 0 is a discrimination of the direction of the initial spine current i_s . The entire comparator measurement, including the preparation of the initial spine current i_s , is repeated at a repetition frequency f_R . A counter accumulates the logic 1 events for f_R trials within a one-second counter window. The normalization of the number of logic 1 counts per second by the repetition frequency is an estimator for the probability of a logic 1 readout and, correspondingly, the direction of the spine current i_s .

The QFP comparator behavior is characterized by its grey zone, illustrated in Figure 6-1(b). One sweeps the spine current, using the spine offset current i_{offset} , and records the probability of a logic 1. In Figure 6-1(b), the probability of logic 1 increases from zero to unity as one increases the spine offset current. The transition between logic 0 and logic 1 occurs at the current i_{s0} . (Note that for an ideal QFP with all components perfectly matched, the current i_{s0} would be zero. QFP nonidealities, for example mismatched arm inductances and critical currents due to variations that arise during fabrication, may be accommodated by the spine offset current and result in a nonzero i_{s0} .) This transition is ideally a discontinuous “step function,” but thermal activation, critical current fluctuations, external flux fluctuations, and other noise sources tend to broaden the transition. The result is the gradual transition from logic 0 to logic 1, called the grey zone. One figure of merit for a comparator is the grey zone slope evaluated at the 50% transition point i_{s0} . The larger the grey zone slope, the closer one’s QFP is to an ideal comparator. The QFP is more sensitive to small changes in the spine current, as induced for example by a qubit, as the slope increases.

The use of a QFP for qubit readout is a straightforward application of the QFP comparator. The QFP is tuned to its 50% point using the spine offset current. The presence of a persistent current qubit induces an additional current into the QFP spine. The direction of this induced qubit current is correlated with the qubit states: a clockwise or counterclockwise persistent current. It is important to note that before the exciter pulse is triggered and the measurement commences, the qubit and the QFP are coherently coupled; the state of the qubit (current circulation direction) and the state of the QFP (current direction along the spine) are entangled. For example, if the qubit is in the state

$$|\Psi_{\text{qubit}}\rangle = c_{\text{cw}}|i_q^{\text{cw}}\rangle + c_{\text{ccw}}|i_q^{\text{ccw}}\rangle \quad (6.1)$$

in which c_{cw} and c_{ccw} are the probability amplitudes of the clockwise and counterclockwise qubit current states, $|i_q^{\text{cw}}\rangle$ and $|i_q^{\text{ccw}}\rangle$, respectively, then the coupled qubit-QFP system is in the entangled state

$$|\Psi_{\text{qubit-QFP}}\rangle = c_{\text{cw}}|i_{\text{q}}^{\text{cw}}; i_{\text{s}}^{\text{up}}\rangle + c_{\text{ccw}}|i_{\text{q}}^{\text{ccw}}; i_{\text{s}}^{\text{down}}\rangle \quad (6.2)$$

The operation of the QFP comparator, as initiated by ramping up the exciter pulse, effectively projects and discriminates the direction of the induced current and, thereby, the projected state of the qubit. In terms of detection, the QFP comparator acts as the quantum probe of the qubit; these two systems become coherently coupled and entangled. The projective measurement is initiated by the large exciter pulse and the admission of a fluxon to the QFP system. The dc SQUID is a subsequent classical measurement of the resulting QFP state. A detailed quantum mechanical description of the measurement process is outside the scope of this report. One may note, however, that the repeated projection of the identically prepared qubit superposition states leads to a probability $|c_{\text{cw}}|^2$ that the QFP measurement indicates a clockwise qubit current, and a probability $|c_{\text{ccw}}|^2$ that it indicates a counterclockwise qubit current. This constitutes a measurement uncertainty in addition to the QFP grey zone. However, unlike the QFP grey zone, the ambiguity due to superposition may be characterized and controlled, as for example in Rabi oscillation experiments.

Recently, we have made experimental efforts to characterize the QFP for use as a persistent-current qubit readout circuit. The characterization included measurements of the QFP comparator grey zone as a function of device temperature, QFP comparator sensitivity, and QFP comparator stability. The grey zone and sensitivity tests are performed using the spine offset current, as illustrated in Figure 6-1(a). The stability test includes the qubit and qubit bias current. The experimental results presented here were performed at Lincoln Laboratory using an Oxford Helium 3 refrigerator equipped with two semi-rigid rf coaxial cables (dc-20 GHz) and four intermediate-frequency flexible coaxial cables (dc-100 MHz). The loaded base temperature measured at the Helium 3 plate is 250 mK.

The QFP grey zone slope as a function of temperature is presented in Figure 6-2. Each point is obtained as illustrated in the inset, which is an example for $T = 2$ K; the slope at the 50% point is obtained by sweeping the spine current with the QFP at the desired temperature. The grey zone slope increases as the temperature decreases because the thermally induced noise sources are suppressed. A grey zone width of approximately 300 nA is reproducibly achieved at 0.3 K, defined as the width achieved by extending the grey zone slope at the probability 0.5 point to the probability 0 and 1 intercepts (see Figure 6-2 inset). However, the grey zone slope improvement saturates at and below ~ 1 K. This may indicate that a noise source with energy scale $k_{\text{B}}T_{\text{T}=1\text{K}}$ still exists in the measurement system. Although quantum tunneling becomes significant at temperatures well below 1 K, a more likely noise source is the on-chip 50- Ω resistor in the exciter line. The exciter line carries current on the order of milliamperes. This corresponds to several 10's to 100's of microwatts of power being dissipated on the chip. Even with a 1–2% duty cycle on the exciter line, the power dissipation may be significant enough to cause local heating. Indeed, the temperature observed at the Helium 3 plate increases from ~ 250 to ~ 300 mK when the exciter line is turned on. The next-generation chip designs eliminate this on-chip resistor.

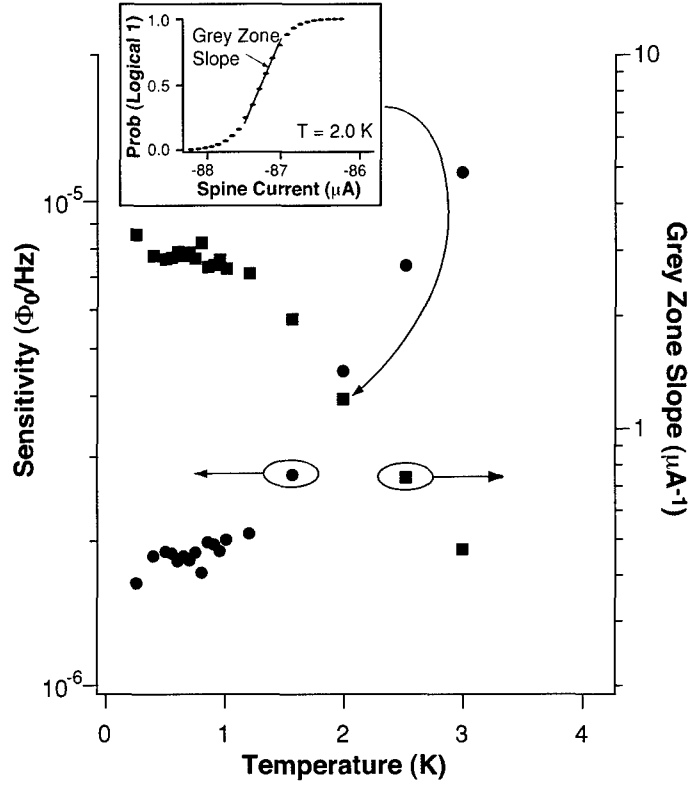


Figure 6-2. Grey zone slope as a function of temperature (right axis). The inset is a grey zone at temperature $T = 2$ K. The slope is the plotted $T = 2$ K point. The corresponding sensitivity is plotted as a function of temperature (left axis). The slope and sensitivity saturate at around 1 K, likely indicating that the on-chip resistor is heating the sample locally.

Intuitively, the smallest fluctuation resolvable by a QFP comparator will decrease as one increases the grey zone slope. In [6], it is shown explicitly that the minimum detectable energy for a QFP comparator is inversely proportional to the slope. Here, the expression is written in units of flux per root hertz as

$$S\left(\frac{\Phi_0}{\sqrt{\text{Hz}}}\right) = \frac{1}{\Phi_0} \sqrt{\frac{2P_1(1-P_1)L^2}{\left(\frac{dP}{dI_s}\right)^2_{P_1} f_R}} \quad (6.3)$$

in which Φ_0 is the quantum unit of flux, P_1 is the probability of a logic 1 at the particular QFP bias point, L is the spine inductance, dP/dI_s is the grey zone slope evaluated at P_1 , and f_R is the repetition frequency of

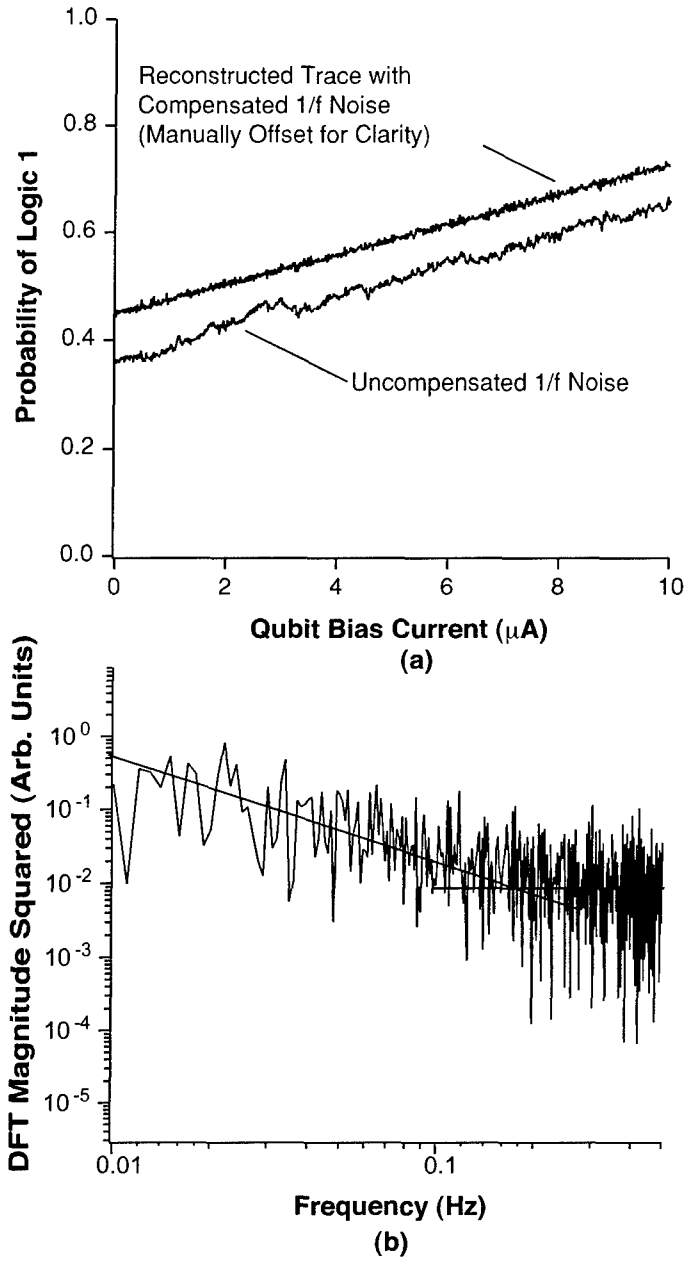


Figure 6-3. (a) Readout of QFP comparator as a function of the qubit bias current (~ 1 -h duration). The data as measured (red trace) exhibits a $1/f$ type noise spectrum. A lock-in type technique is used to remove this low-frequency fluctuation (blue trace). Traces are offset for clarity in presentation. The general increase in probability of logic 1 is due to the mutual coupling of the qubit bias current to the spine. (b) Power spectrum for the uncompensated data in (a) with the mutual coupling contribution removed. The data exhibit a $1/f$ type noise with a corner frequency of 200 mHz, corresponding to a characteristic time of 5 s.

the measurement. The QFP is most sensitive when biased at the 50% point ($P = 0.5$); this is the point of steepest grey zone slope, and it maximizes the $P_1(1-P_1)$ factor in Equation (6.3). In Figure 6-1, using the slope-vs-temperature data (right axis), one finds the corresponding flux noise sensitivity (left axis). The saturation value in these units is $S_{\text{sat}} = 1.8 \times 10^{-6} \Phi_0 / \sqrt{\text{Hz}}$, a value comparable to a dc SQUID detector assuming ideal flux coupling to the spine.

The readout concept for a qubit is the following: one biases the QFP at or near $P_1 = 0.5$, and the induced current on the spine due to the qubit will drive the comparator towards digital “0” or digital “1” depending on the projected qubit state. The approach is predicated on the assumption of QFP stability. That is, the QFP should not make a “random walk” away from the linear region about the $P_1 = 0.5$ bias point while a measurement is being undertaken. Such a random walk could occur, for example, if the spine current i_{s0} carries temporal fluctuations due to external flux fluctuations, trapped flux fluctuations, or critical current fluctuations in the QFP. This is particularly important in the limit that the induced spine current from the qubit is small compared with the grey zone transition region.

As an example of QFP comparator stability, Figure 6-3(a) presents the repeated measurement of the QFP state as a function of the qubit bias current. The duration of the experiment is approximately 1 h. The qubit is flux biased using a nearby wire carrying a qubit bias current, as seen in Figure 6-1(a). The red trace in Figure 6-3(a) is the resulting uncompensated QFP readout; the blue trace is the reconstructed readout. Two characteristics stand out. First, both traces exhibit an increase in logic 1 probability with the qubit bias current. This is due to mutual coupling between the qubit bias line and the QFP spine, and it is not a $1/f$ walkoff. Second, the uncompensated trace in Figure 6-3(a) does exhibit a $1/f$ type noise. The power spectrum of the uncompensated trace, without the mutual coupling contribution, is presented in Figure 6-3(b). The power spectrum exhibits a $1/f$ corner at ~ 0.2 Hz, corresponding to a time scale of ~ 5 s. To remedy this, a lock-in type of measurement is performed “manually.” For each time step, two measurements are made: one is the point of interest, and the second is a reference point. The time required to perform both measurements is < 3 s, which is smaller than the $1/f$ time scale. Thus, $1/f$ fluctuations are assumed to affect the point of interest and the reference point identically; by subtracting off the common $1/f$ noise contribution, the *measurement* stability is greatly improved. The trace in Figure 6-3(b) is the reconstructed version of the trace in Figure 6-3(a). Note that the penalty incurred for correcting the $1/f$ noise by subtracting two signals is a $\sqrt{2}$ increase in the residual rms current fluctuations (the residual fluctuations are assumed to be uncorrelated). The rms spine current fluctuations are approximately a factor of 10 smaller than the expected change in induced spine current because of a change in the qubit state, as determined through simulation. Therefore, the present level of sensitivity should be sufficient to observe the two qubit states.

Thus, the QFP comparator is a promising readout element for a persistent current qubit. The QFP grey zone width decreases as the temperature is decreased; a width of 300 nA is achieved reproducibly at temperatures of 300 mK. This corresponds to sensitivity of approximately $S_{\text{sat}} = 1.8 \times 10^{-6} \Phi_0 / \sqrt{\text{Hz}}$, which is comparable to the sensitivity of dc SQUIDS. The $1/f$ noise associated with the QFP occurs on time scales of ~ 5 s, and it is effectively removed using a lock-in type technique. The remaining fluctuations in the qubit readout are a factor 10 smaller than the estimated qubit signal. Future work includes performing

qubit level “spectroscopy” using the QFP comparator at Helium 3 temperatures and, ultimately, at 10 mK in a dilution refrigerator.

W. D. Oliver	K. K. Berggren
J. P. Sage	T. P. Orlando*
T. J. Weir	R. L. Slattery
G. Fitch	

REFERENCES

1. J. E. Mooij, T. P. Orlando, L. Levitov, L. Tian, C. H. van der Wal, and S. Lloyd, *Science* **285**, 1036 (1999).
2. T. P. Orlando, J. E. Mooij, L. Tian, C. H. van der Wal, L. S. Levitov, S. Lloyd, and J. J. Mazo, *Phys. Rev. B* **60**, 15398 (1999).
3. C. H. van der Wal, A. C. J. ter Haar, F. K. Wilhelm, R. N. Schouten, C. J. P. M. Harmans, T. P. Orlando, S. Lloyd, and J. E. Mooij, *Science* **290**, 773 (2000).
4. I. Chiorescu, Y. Nakamura, C. J. P. M. Harmans, and J. E. Mooij, *Science* **299**, 1869 (2003).
5. K. Nakane and E. Goto, in *Fluxoid Josephson Computer Technology*, E. Goto, T. Soma, and L. K. Fock, eds. (World Scientific, Singapore, 1988), pp. 12–14.
6. D. A. Feld, J. P. Sage, K. K. Berggren, and A. Siddiqui, *IEEE Trans. Appl. Supercond.* **9**, 4361 (1999).

*Author not at Lincoln Laboratory.

7. ADVANCED SILICON TECHNOLOGY

7.1 NEW SPICE MODEL UTILIZING THE BODY-SOURCE BUILT-IN POTENTIAL LOWERING OF SOI MOSFETS

As silicon-on-insulator (SOI) technology matures [1]–[3] for low-voltage and low-power applications, inadequate modeling of the floating-body phenomenon is the main obstacle that hinders SOI design [3]–[6]. One important floating-body phenomenon is impact-ionization charging, counter balanced by self-biasing of the body-source junction. A recent report [7] on the interpretation of low-voltage impact ionization indicates that the body-charging mechanism remains significant with scaling. The degree of the resulting floating-body effect is consequently determined by the built-in potential of the body-source junction.

The body-source potential barrier (the built-in potential V_{bi}) causes the accumulation of majority carriers and hence induces the floating-body effect [8]–[10]. This barrier exists in both partially depleted (PD) and fully depleted (FD) devices. The only difference between the two is that the FD device has a built-in potential lowering, ΔV_{bi} , and therefore a smaller potential barrier height than the PD device. In other words, ΔV_{bi} is an index of the degree of full depletion.

Here, we investigate SOI metal-oxide-semiconductor field effect transistors (MOSFETs) from the angle of the body-source built-in potential lowering, which has rarely been experimentally tackled. This characterization serves as a basis for the compact modeling of ΔV_{bi} . Moreover, we address the need to link PD and FD SOI models using the concept of ΔV_{bi} for state-of-the-art SOI technologies. Accurate compact models, i.e., SPICE models, for PD transistors and for transistors that are FD under *all conditions* already exist. What we have developed is a unified model that represents the full range of depletion.

A direct probe of ΔV_{bi} can be achieved by finding the onset of the external body bias, through a body contact, above which the threshold voltage V_T and hence the channel current of the FD SOI device is modulated. Notice that this onset voltage is negative for PD devices. (Throughout this report we refer to *n*-channel transistors. For *p*-channel, all polarities are reversed.) As shown in Figure 7-1, ΔV_{bi} is induced by the vertical capacitive coupling from front gate V_{GS} to back gate V_{bGS} , and can be formulated by applying the Poisson equation in the vertical direction [11]. ΔV_{bi} increases as the channel doping N_{ch} or SOI thickness T_{Si} decreases, as shown in Figure 7-2. Notice that ΔV_{bi} is linearly dependent on N_{ch} with a slope proportional to T_{Si}^2 , as predicted by the Poisson equation.

Besides the vertical coupling, ΔV_{bi} may be raised by additional charge sharing [12] from source and drain electrode through the SOI buried oxide, an inherent feature of FD MOSFETs. As shown in Figure 7-3(a), ΔV_{bi} rolls up while V_T rolls off [13] as the gate length is scaled down because of drain field penetration. Also notice the reduction of the back-gate effect on ΔV_{bi} owing to the same mechanism, as shown in Figure 3(b). The enhanced ΔV_{bi} due to charge sharing suppresses further the floating-body effect in short-channel FD devices [14]–[16], which may determine the transistor off-state leakage.

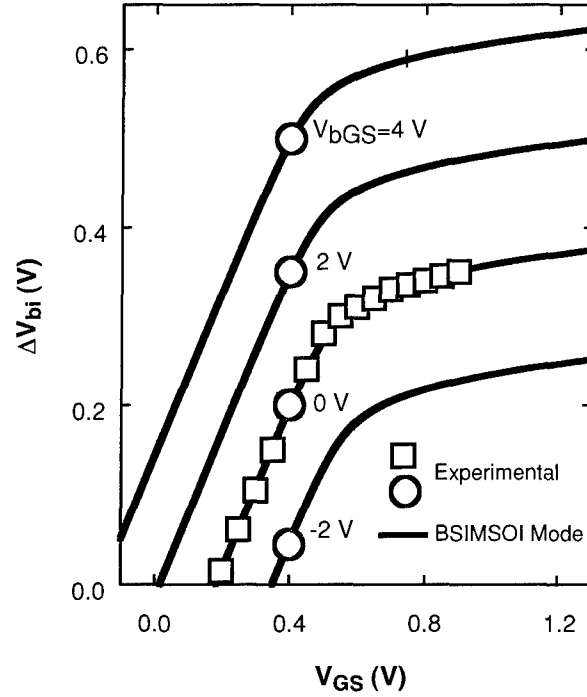


Figure 7-1. ΔV_{bi} vs V_{GS} . ΔV_{bi} is caused by vertical coupling from front gate to back gate. It can be experimentally determined using body-contacted devices. $L_G = 0.5 \mu\text{m}$, $T_{Si} = 40 \text{ nm}$, $N_{ch} = 6 \times 10^{17} \text{ cm}^{-3}$, $T_{BOX} = 200 \text{ nm}$.

The importance of ΔV_{bi} to state-of-the-art high-performance SOI technologies lies in the tendency toward full depletion due to aggressive SOI thickness scaling [17]–[19]. Specifically, the need for transistors with different threshold voltages and oxide thicknesses in a single chip may result in the coexistence of both PD and FD devices in the same circuit by design. Furthermore, the laterally nonuniform channel doping created by modern halo implants may lead to PD nominal devices and FD long-channel devices with continuous variations in between. Since these medium- to long-channel FD devices are potential replacements of body-contacted devices, a compact SOI model continuously spanning PD and FD is needed for SOI circuit design. The concept of body-source built-in potential lowering enables us to capture all these scaling trends.

Therefore, we have linked PD and FD using the ΔV_{bi} concept. Under the framework of the industry standard [20] PD SOI model, BSIMPD [21], ΔV_{bi} has been incorporated in the diode current model in an exponential manner to determine the body potential. As shown in Figure 7-4, for a given significant ΔV_{bi} (e.g., 0.52 V), the body-source diode can sink a huge amount of body charge injection (e.g., impact ionization) without varying the body potential. In other words, the transistor threshold voltage remains constant as long as the vertical coupling ΔV_{bi} is strong enough to hold the potential inside the body.

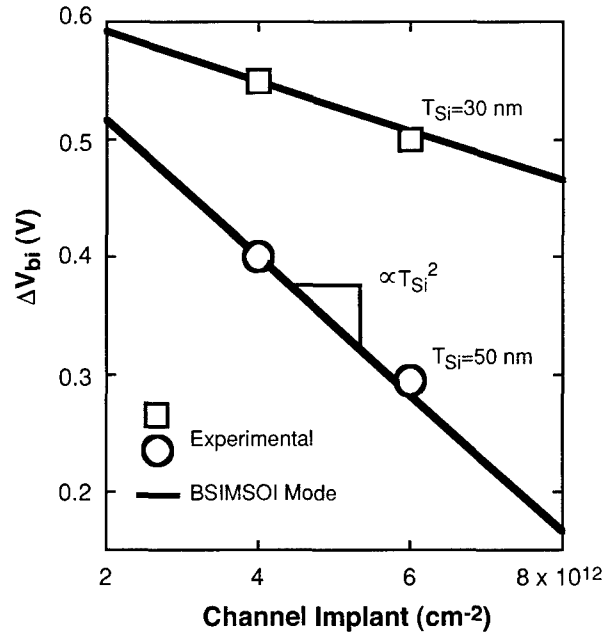


Figure 7-2. ΔV_{bi} vs channel implant. ΔV_{bi} depends linearly on channel doping with a slope proportional to T_{Si}^2 . It is an index of the degree of full depletion. $L_G = 1 \mu m$, $T_{BOX} = 85 \text{ nm}$, $V_{GS} = 0.1 \text{ V}$, $V_{bGS} = 0 \text{ V}$.

Contrarily, for the PD device without built-in potential lowering (i.e., $\Delta V_{bi} = 0 \text{ V}$), the body potential is always changed as a function of the body-to-source current. Notice that even FD devices exhibit the floating-body effect to varying degrees, dependent on the level of majority carrier injection and ΔV_{bi} .

This unified SOI model, BSIMSOIv3.0 [11], approaches the PD model when ΔV_{bi} is negligible in the ON state, while it returns to the ideal FD model, without the floating-body effect, when ΔV_{bi} is significant even when the transistor is OFF. Thus, the ΔV_{bi} value can be used to determine the need for floating-body simulation to increase efficiency [21]. In addition, ΔV_{bi} may be used as a criterion for determining the degree of full depletion in the optimization of SOI devices. The SOI device may be designed to have a significant ΔV_{bi} and hence negligible history effect for the ease of circuit design and reduction of simulation computation time.

This new model, developed by collaborators at the University of California at Berkeley, has been used to simulate the FD SOI transistors built in the Lincoln Laboratory 180-nm CMOS process. Example drain characteristics are shown in Figure 7-5. The kink effect, due to body charging, is apparent in the long-channel ($0.5 \mu m$) device. This kink is absent in the short-channel ($0.18 \mu m$) device because of the larger ΔV_{bi} value discussed above. The simulation fits the measured data rather well.

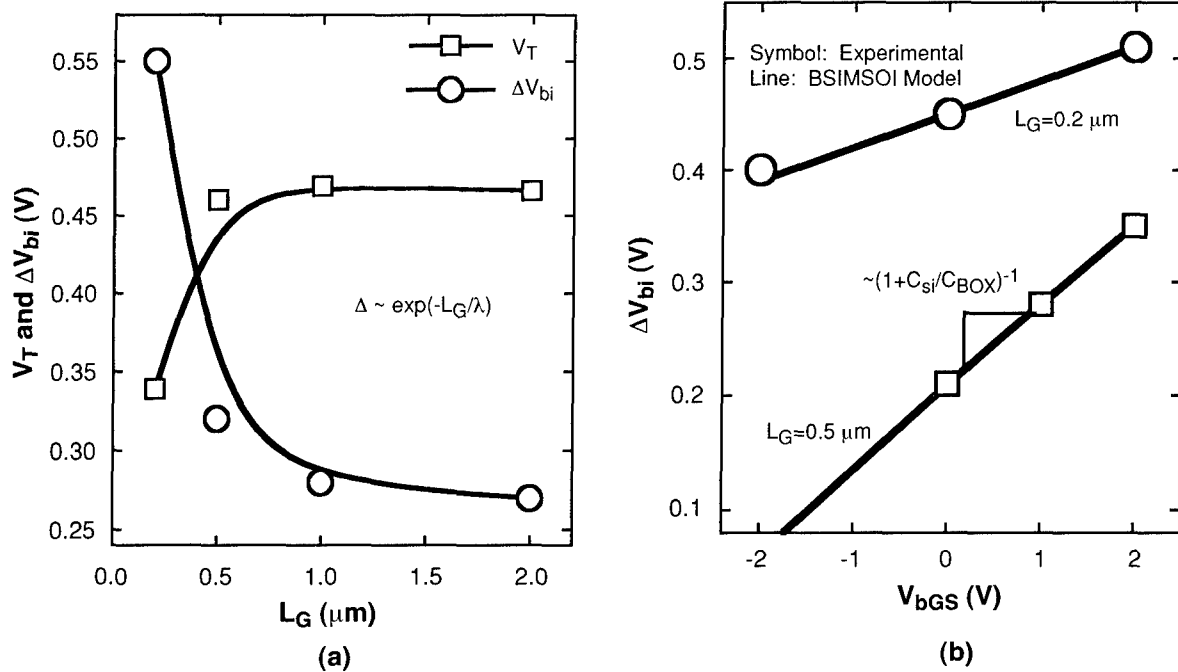


Figure 7-3. (a) V_T and ΔV_{bi} vs L_G . Drain field penetration causes roll-off and raises ΔV_{bi} for the short-channel device. (b) ΔV_{bi} vs V_{bGS} . Back-gate effect on ΔV_{bi} (the slope in this figure) for the short-channel device is also reduced because of the charge sharing. C_{BOX} is the buried oxide capacitance, and C_{Si} is the capacitance of the depleted SOI silicon film. $V_{GS} = 0.4$ V, $T_{Si} = 40$ nm, $N_{ch} = 6 \times 10^{17} \text{ cm}^{-3}$, $T_{BOX} = 200$ nm.

The body-source built-in potential lowering is the main difference between PD and FD SOI MOSFETs, as well as the connection between the two types of device. This physical measure not only serves as an index of the floating-body behavior of SOI devices but also enables the unification of PD and FD models. The new, unified compact model reported here will help to enable the trend toward coexistence of PD and FD devices in a single chip and therefore to continue the scaling of SOI CMOS.

P. Su*	S. K. H. Fung*
P. W. Wyatt	H. Wan*
A. Niknejad*	M. Chan*
C. Hu*	

*Author not at Lincoln Laboratory.

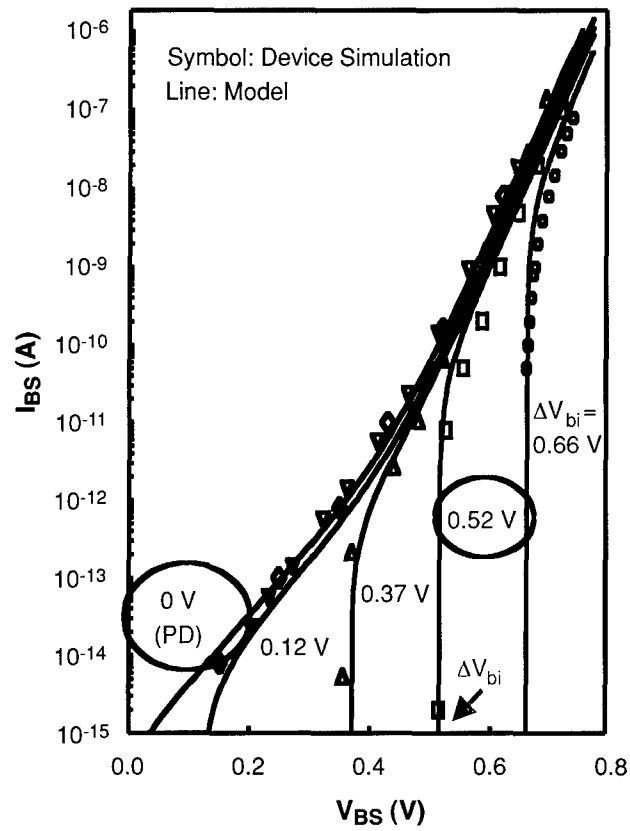


Figure 7-4. I_{BS} vs V_{BS} . ΔV_{bi} determines the diode current-voltage and therefore the body potential of silicon-on-insulator (SOI) devices. It is the link between partially depleted (PD) and fully depleted models.

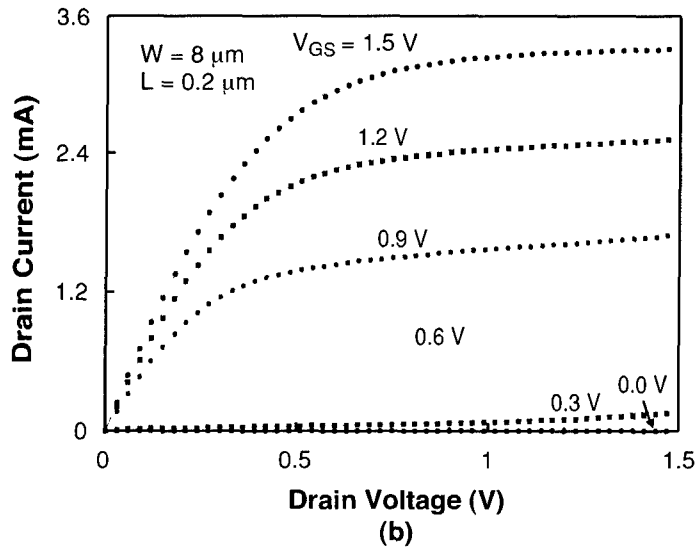
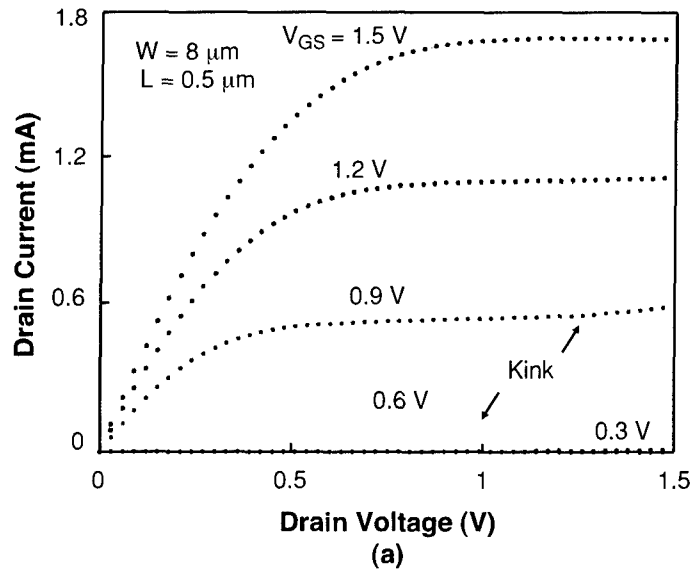


Figure 7-5. Measured (points) and simulated (lines) current-voltage curves for two transistors from Lincoln Laboratory's fully depleted SOI CMOS process.

REFERENCES

1. G. Shahidi, A. Ajmera, F. Assaderaghi, E. Leobandung, D. Sankus, W. Rausch, D. Schepis, L. Wagner, K. Wu, and B. Davari, *International Solid-State Circuits Conference Technical Digest* (IEEE, Piscataway, N.J., 1999), p. 426.
2. S. K. H. Fung, N. Zamdmer, P. J. Oldiges, et al., *International Electron Devices Meeting Technical Digest* (IEEE, Piscataway, N.J., 2000), p. 231.
3. J. L. Pelloie, C. Raynaud, O. Faynot, A. Grouillet, and J. Du Port de Pontcharra, *Microelectron. Eng.* **48**, 327 (1999).
4. C.-T. Chuang, P.-F. Lu, and C. J. Anderson, *Proc. IEEE* **86**, 689 (1998).
5. F. Assaderaghi, G. G. Shahidi, S. Fung, M. Sherony, L. Wanger, J. Sleight, S. H. Lo, K. Wu, and T.-C. Chen, *Proceedings of the 12th International Conference on Microelectronics* (IEEE, Piscataway, N.J.), p. 201.
6. K. Shepard and D.-J. Kim, *IEEE Trans. Computer-Aided Design* **20**, 888 (2001).
7. P. Su, K. Goto, T. Sugii, and C. Hu, *IEEE Electron Device Lett.* **23**, 550 (2002).
8. J.-P. Colinge, *IEEE Electron Device Lett.* **EDL-9**, 97 (1988).
9. F. Balestra, T. Matsumoto, M. Tsuno, H. Nakabayashi, Y. Inoue, and M. Koyanagi, *Electron. Lett.* **31**, 326 (1995).
10. K. Hui, M. Chan, F. Assaderaghi, C. Hu, and P. Ko, *Proceedings of IEEE International SOI Conference* (IEEE, Piscataway, N.J., 1994), p. 65.
11. BSIMSOI Users' Manual. (<http://www-device.eecs.Berkeley.edu/~bsimsoi>)
12. L. Su, J. Jacobs, J. Chung, and D. Antoniadis, *IEEE Electron Device Lett.* **15**, 366 (1994).
13. Z. Liu, C. Hu, J. Huang, T. Chan, M. Jeng, P. Ko, and Y. Cheng, *IEEE Trans. Electron Devices* **40**, 86 (1993).
14. T. Tsuchiya, Y. Sato, and M. Tomizawa, *IEEE Trans. Electron Devices* **45**, 1116 (1998).
15. J. W. Sleight and R. Rios, *International Electron Devices Meeting Technical Digest* (IEEE, Piscataway, N.J., 1996), p. 143.
16. J. Fossum, S. Krishnan, O. Faynot, S. Cristoloveanu, and C. Raynaud, *IEEE Electron Device Lett.* **16**, 542 (1995).

17. R. Chau, J. Kavalieros, B. Doyle, A. Murthy, N. Paulsen, D. Lionberger, D. Barlage, R. Arghavani, B. Roberds, and M. Doczy, *International Electron Devices Meeting Technical Digest* (IEEE, Piscataway, N.J., 2001), p. 621.
18. S. K. H. Fung, M. Khare, D. Schepis, et al., *International Electron Devices Meeting Technical Digest* (IEEE, Piscataway, N.J., 2001), p. 629.
19. H. Wan, S. Fung, P. Su, M. Chan and C. Hu, *Proceedings of IEEE International SOI Conference* (IEEE, Piscataway, N.J., 2002), p. 140.
20. <http://www.eigroup.org/cmc>
21. P. Su, S. Fung, S. Tang, F. Assaderaghi, and C. Hu, *Proceedings of IEEE Custom Integrated Circuits Conference* (IEEE, Piscataway, N.J., 2000), p. 197.